

Ice Particle Properties Inferred from Aggregation Modelling

Markus Konrad Karrer¹, Stefan Kneifel², Davide Ori³, Christoph Siewert⁴, Axel Seifert⁴,
and Annakaisa von Lerber⁵

¹Institute of Geophysics and Meteorology

²University of Cologne

³Institute for Geophysics and Meteorology

⁴Deutscher Wetterdienst

⁵Finnish Meteorological Institute

November 30, 2022

Abstract

We generated a large number (105'000) of aggregates composed of various monomer types and sizes using an aggregation model. Combined with hydrodynamic theory, we derived ice particle properties such as mass, projected area, and terminal velocity as a function of monomer number and size. This particle ensemble allows us to study the relation of particle properties with a high level of detail which is often not provided by in-situ measurements. The ice particle properties change rather smoothly with monomer number. We find very little differences in all particle properties between monomers and aggregates at sizes below 1 mm which is in contrast to many microphysics schemes. The impact of the monomer type on the particle properties decreases with increasing monomer number. Whether e.g., the terminal velocity of an aggregate is larger or smaller than an equal-size monomer, depends mostly on the monomer type. We fitted commonly used power laws as well as Atlas-type relations, which represent the saturation of the terminal velocity at larger sizes, to the dataset and tested the impact of incorporating different levels of complexity with idealized simulations using a 1D Lagrangian super-particle model. These simulations indicate that it is sufficient to represent the monomer number dependency of ice particle properties with only two categories (monomers and aggregates). The incorporation of the saturation velocity at larger sizes is found to be important to avoid an overestimation of self-aggregation of larger snowflakes.

Ice Particle Properties Inferred from Aggregation Modelling

M. Karrer¹, A. Seifert², C. Siewert², D. Ori¹, A. von Lerber^{1,3}, S. Kneifel¹

¹Institute for Geophysics and Meteorology, University of Cologne, Cologne, Germany

²Deutscher Wetterdienst, Offenbach, Germany

³Finnish Meteorological Institute, Helsinki, Finland

Key Points:

- We simulated aggregates to study the impact of monomer number and type on ice particle properties
- Ice particle properties show a smooth transition from monomers to aggregates
- The saturation of terminal velocity needs to be taken into account when simulating snow aggregation

Abstract

We generated a large number (105'000) of aggregates composed of various monomer types and sizes using an aggregation model. Combined with hydrodynamic theory, we derived ice particle properties such as mass, projected area, and terminal velocity as a function of monomer number and size. This particle ensemble allows us to study the relation of particle properties with a high level of detail which is often not provided by in-situ measurements. The ice particle properties change rather smoothly with monomer number. We find very little differences in all particle properties between monomers and aggregates at sizes below 1 mm which is in contrast to many microphysics schemes. The impact of the monomer type on the particle properties decreases with increasing monomer number. Whether e.g., the terminal velocity of an aggregate is larger or smaller than an equal-size monomer, depends mostly on the monomer type. We fitted commonly used power laws as well as Atlas-type relations, which represent the saturation of the terminal velocity at larger sizes, to the dataset and tested the impact of incorporating different levels of complexity with idealized simulations using a 1D Lagrangian super-particle model. These simulations indicate that it is sufficient to represent the monomer number dependency of ice particle properties with only two categories (monomers and aggregates). The incorporation of the saturation velocity at larger sizes is found to be important to avoid an overestimation of self-aggregation of larger snowflakes.

Plain Language Summary

We have simulated and analyzed the properties, such as mass, area, and terminal fall velocity of snowflakes using a computer model. The snowflakes in the atmosphere form by collisions of ice crystals present in many different shapes. In the computer model, ice crystals shapes typically found in the atmosphere, are stuck together to create three-dimensional snowflakes. The properties of the snowflakes depend on the shape and the number of ice crystals that are stuck together. While in weather and climate models the properties of ice crystals and snowflakes are often assumed to be very different even if they are of the same size, we find very little differences in their properties. Many weather and climate models assume that snowflakes have a higher fall velocity the larger they are, although field observations have shown that particles larger than a few mm all fall with similar velocity. We fitted new parameterizations of the particle velocities which can remove this deficiency in the models. Finally, we used another model and showed

45 that it might be sufficient to divide the properties of the ice particles in only two cat-
 46 egories. However, it is important to consider the almost constant velocity of the large
 47 snowflakes.

48 **1 Introduction**

49 The terminal velocity v_{term} of ice monomers and aggregated ice particles and its
 50 relation to size has manifold impacts on precipitation and radiative effects of ice contain-
 51 ing clouds. For example, Morales et al. (2019) show that parameters describing v_{term}
 52 of aggregates have the largest impact on the precipitation of simulated orographic clouds.
 53 Experiments with global climate simulations revealed that also radiative fluxes are very
 54 sensitive to changes in v_{term} (Jakob, 2002). Sanderson et al. (2008) found, that v_{term}
 55 of ice is the second most influential parameter for the climate sensitivity in their multi-
 56 member perturbed physics General Circulation Model ensemble. Constraining v_{term} of
 57 cloud ice and aggregated ice particles can reduce the degrees of freedom in model tun-
 58 ing (e.g., to improve top of atmosphere radiative fluxes; Schmidt et al., 2017) and im-
 59 prove the physical consistency in atmospheric models.

60 The importance of v_{term} of ice particle has been early recognized and has motivated
 61 first observational studies in the first third of the 20th century. Using initially manual
 62 observations and microphotography, pioneering studies such as Nakaya and Terada (1935);
 63 Langleben (1954); Brown (1970); Zikmunda and Vali (1972); Kajikawa (1972); Locatelli
 64 and Hobbs (1974) investigated the relation of v_{term} to the particle’s size for various ice
 65 particle habits and aggregates. In addition to the direct measurements of velocity, sev-
 66 eral studies started to investigate the principle relation between particle properties such
 67 as mass, size, and projected area to v_{term} which allows deriving v_{term} from these quan-
 68 tities (Cornford, 1965; Heymsfield, 1972). Due to the large efforts in performing these
 69 often manual measurements, the sample size of the derived relations is rather small. For
 70 example, some of the relations of the widely used relations by Locatelli and Hobbs (1974)
 71 are only based on 10 to 50 particles. One can assume that particles with ideal monomer
 72 types might have been subjectively chosen in order to easier associate the derived rela-
 73 tionships to certain well defined shapes. Nevertheless, the relations of size, mass, area,
 74 and v_{term} derived in these early studies are still used in microphysics parameterizations
 75 (e.g. the v_{term} -size relation of the snow category in Morrison and Milbrandt (2015) is
 76 taken from Locatelli and Hobbs (1974) mixed aggregates; see Figure 1). In Figure 1a a

77 selection of the aforementioned v_{term} relations are shown for their defined size range. The
 78 spread of velocities for different ice particle monomers is relatively high (e.g. Kajikawa
 79 (1972) reported v_{term} to be about 0.2 m s^{-1} for a dendrite but about 0.5 m s^{-1} for a
 80 plate monomer). In contrast, v_{term} of aggregates of different monomer types appear to
 81 be relatively similar and always close to 1 m s^{-1} in the reported size range.

82 Evolving computer technology allowed the realization of automated particle mea-
 83 surement systems such as the 2D Video Disdrometer (2DVD, Kruger and Krajewski (2002)),
 84 the Snow video imager (SVI; Newman et al., 2009), its successor the Particle Imaging
 85 Package (PIP Tiira et al., 2016), the Hydrometeor Velocity and Shape Detector (HVSD;
 86 Barthazy et al., 2004), or the multi-angle snowflake camera (MASC; Garrett et al., 2012).
 87 These systems are based on optical methods to capture particle size and terminal veloc-
 88 ity. Unlike in the early studies, particle property relations (Barthazy & Schefold, 2006;
 89 Brandes et al., 2008; Zawadzki et al., 2010; Garrett & Yuter, 2014b) are now based on
 90 a very large number of particles which are classified by automated algorithms rather than
 91 visual selection (Bernauer et al., 2016; von Lerber et al., 2017). Some of the systems have
 92 limitations regarding the smallest detectable particle size (e.g., 0.1–0.2 mm for 2DVD)
 93 which suggests the results to be in general more reliable for larger particles. A general
 94 behavior which is revealed by all instruments is a 'saturation' of aggregate terminal ve-
 95 locities at approximately 1 m s^{-1} for unrimed particles and sizes larger than a few mil-
 96 limeters (Figure 1a).

97 Most ice microphysics schemes use two categories for unrimed ice particles which
 98 are commonly denoted as cloud ice and snow/aggregates. Relations between particle prop-
 99 erties such as size (e.g. the maximum dimension D_{max}), mass m , projected area A , or
 100 v_{term} are defined for each category. Examples of the v_{term} dependence on size which are
 101 implemented in widely used two-moment schemes are shown in Figure 1b. When com-
 102 paring these relations with observations (Figure 1a), we miss the saturation behavior of
 103 v_{term} for larger sizes in most relations. This discrepancy is expected as most schemes
 104 use power laws, which are unable to represent a saturation behavior. Alternative 'Atlas-
 105 type' three-parameter fits have been suggested (Seifert et al., 2014) but so far they have
 106 not been tested thoroughly. A newer scheme, the Predicted Particle Properties (P3) scheme
 107 (Morrison & Milbrandt, 2015), that only uses one ice category and a look-up table ap-
 108 proach for v_{term} is also better able to capture the saturation at large sizes. At the smaller
 109 size range, the snow category is found for all schemes to fall significantly faster than the

110 ice category with the same size. Considering that v_{term} depends strongly on m and A
111 of the particle, it might sound plausible, that for example, an aggregate of a few plates
112 should fall faster than a single plate of the same size. Unfortunately, most observations
113 do not provide sufficiently detailed information about monomer number and type which
114 would be needed to answer the question of whether there exists a 'jump' in v_{term} for the
115 number of monomers exceeding a certain threshold. Many observational datasets are even
116 lacking a direct measurement of the particles' m and A .

117 An interesting new tool to better understand the underlying principles of aggre-
118 gation and its effects on particle properties are aggregation models (Westbrook et al.,
119 2004a; Hashino & Tripoli, 2011; Leinonen et al., 2012; Ori et al., 2014; Przybylo et al.,
120 2019). Those models use idealized monomer shapes (e.g., dendrites, needles, plates, columns)
121 with particle properties matched to in-situ observations. Aggregates simulated with the
122 model by Westbrook et al. (2004a) helped to better understand theoretical scaling re-
123 lations associated to aggregation such as the increase of aggregate mass with size by a
124 power of two (Westbrook et al., 2004b), which was known from several previous in-situ
125 observations. This model has been extended by Leinonen et al. (2012) providing a large
126 number of monomer shapes and also provides an option to rime the aggregate (Leinonen
127 & Szyrmer, 2015). This allowed to better understand the evolution of size and mass of
128 a large number of aggregates which were increasingly rimed (Seifert et al., 2019).

129 To infer v_{term} from modeled ice particles or aggregates, computational fluid dy-
130 namics is an accurate but also computational costly method. It has been recently ap-
131 plied to idealized ice particle shapes (Hashino et al., 2016; Nettesheim & Wang, 2018;
132 Bürgesser et al., 2019) and more computations with more complex shapes can be expected
133 shortly. Hydrodynamic theory is a computational cheaper alternative to calculate v_{term}
134 based on a number of bulk particle characteristic, rather than the complex 3D-shape (e.g.
135 Böhm, 1992; Khvorostyanov & Curry, 2005; Heymsfield et al., 2010). The accuracy of
136 hydrodynamic theories has recently been evaluated by ice particle analogs falling in an
137 oil tank (Westbrook & Sephton, 2017). The experimental results show deviations smaller
138 than 20% for the Heymsfield et al. (2010) theory. A problematic aspect of these theo-
139 ries is still the formulation of the scaling towards higher Reynolds number (i.e. large par-
140 ticles) and the simulation of more complex particle shapes.

141 Aggregation models in combination with hydrodynamic theory have recently been
 142 used to study v_{term} of aggregates (Hashino & Tripoli, 2011; Schmitt et al., 2019). Hashino
 143 and Tripoli (2011) identified a dependency of the aggregation rate and aggregate mass
 144 on the mean size and type of the monomers. Schmitt et al. (2019) analyzed v_{term} and
 145 its variability of simulated aggregates composed of hexagonal prisms taken from a monodis-
 146 perse monomer size distribution. They found that the variability of v_{term} is caused by
 147 the variability of the number of monomers N_{mono} and the monomers' aspect ratio.

148 In this study, we aim to study the dependency of m , A and v_{term} on size, monomer
 149 number and type. For this, we create a large number of aggregates with various monomer
 150 types including also mixtures of different monomer types. The monomer size is sampled
 151 from a size distribution rather than a constant size to better represent real ensembles
 152 of aggregates. Central questions of this study are, how important is the monomer num-
 153 ber and type information for parameterizing aggregate properties and how well can they
 154 be parameterized by different functional relations?

155 To answer these questions, we describe in Section 2 the aggregation model and the
 156 created dataset of unrimed aggregates as well as the hydrodynamic theory to calculate
 157 v_{term} based on m and A of these particles. The simulated particle properties are com-
 158 pared to in-situ observations in Section 3. Section 4 presents several parameterizations
 159 of the particle properties. Finally, in Section 5, we use a 1D Lagrangian particle model
 160 to test the impact of including different complexity of particle properties for aggrega-
 161 tion

162 **2 Methods**

163 **2.1 Aggregation model**

164 We use the aggregation model developed by Leinonen (2013) which includes a large
 165 number of realistic monomers (hexagonal plates, dendrites, columns, needle). Originally,
 166 the aggregation model was designed to produce realistic snow particle structures which
 167 can then be used to calculate their scattering properties (Leinonen & Moisseev, 2015;
 168 Leinonen et al., 2018). The model has also been used to systematically investigate mi-
 169 crophysical processes such as riming (Seifert et al., 2019).

170 The shape characteristics (length, thickness, etc.) of the monomers are predefined
 171 by geometric relations based on in-situ observations (Leinonen & Moisseev, 2015). The

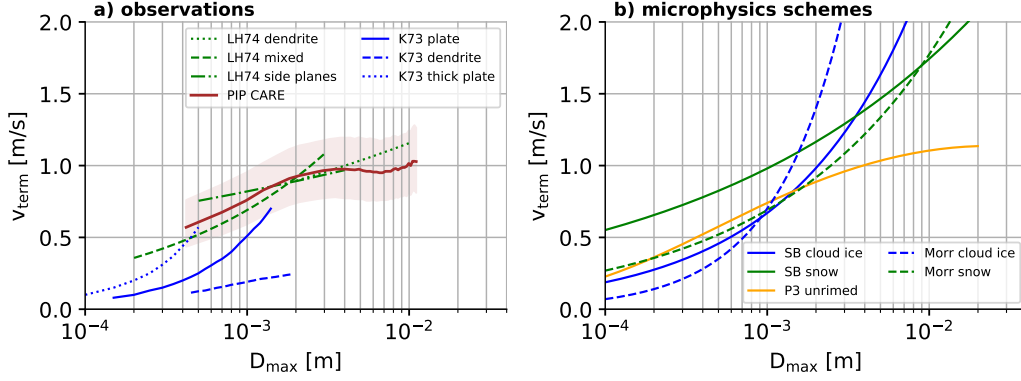


Figure 1. a) In-situ measurements of v_{term} of monomers (separated by monomer type; Kajikawa (1972, blue)) and aggregates composed of different monomers (green: Locatelli and Hobbs (1974, LH74)) and particle ensembles from the PIP-CARE dataset (see Section A1). b) v_{term} of unrimed ice particles in two-moment microphysics schemes. The blue line represents the implementation of cloud ice (monomers), the green line the implementation for the snow (aggregates) category in Seifert and Beheng (2006, solid lines, SB) and Morrison et al. (2005, dashed lines, Morr). The Predicted Particle scheme (Morrison & Milbrandt, 2015, P3) assumes identical properties for all unrimed particles (yellow line).

172 aggregation process starts with generating N_{mono} monomers with sizes following a pre-
 173 defined inverse exponential probability density function $p_d(D_{max})$

$$p_d(D_{max}) = \lambda \exp(-\lambda D_{max}) \quad (1)$$

174 where λ^{-1} is the size parameter of the monomer distribution and D_{max} is the maximum
 175 size of the monomer. The higher λ^{-1} the larger are the sizes of the monomers.

176 The monomers sizes are sampled from the monomer distribution and assembled un-
 177 til an aggregate, consisting of N_{mono} monomers is build up. In each aggregation step,
 178 pairs of particles are selected and the thereby formed aggregate is one of the candidates
 179 for the next aggregation step. The selection of these particle pairs considers a simpli-
 180 fied gravitational collection kernel. During the aggregation process, the collecting par-
 181 ticles are partially aligned with the principal axis in the x-y plane. Rotations around the
 182 principal axis are performed randomly with a standard deviation of 40° . The collected
 183 particles are randomly aligned, which mimics the complex flow in the vicinity of other
 184 particles (Leinonen & Moisseev, 2015).

185 The aggregation simulations performed in this study differ from previous studies
 186 in two main aspects. The first aspect is the resolution of the particle structure. The par-
 187 ticle is internally represented by a three-dimensional lattice with a predefined distance
 188 of the volume elements of typically $40 \mu\text{m}$. This distance was found to be sufficiently small
 189 for scattering computations while being coarse enough in order to keep the numerical
 190 costs for the scattering computations in a reasonable range. However, we discovered, that
 191 for small particle sizes, the theoretical relations for certain particle properties (see Fig-
 192 ure 1 in Leinonen and Moisseev (2015)) are not exactly matched by the discretized par-
 193 ticle. This discrepancy can be easily explained when considering for example that plate
 194 monomers with $D_{max} < 3.03 \text{ mm}$ consist of only one layer of volume elements if the de-
 195 fault resolution of $40 \mu\text{m}$ is used. This does not necessarily affect the aggregate prop-
 196 erties of those monomers as shown in Leinonen and Moisseev (2015), however, in our study,
 197 the focus is to investigate the transition from small to larger sizes particles. Hence, we
 198 need to refine the resolution especially for small particles.

199 As a compromise between computational feasibility and having fine enough resolved
 200 particles, aggregates with $N_{mono} \leq 100$ are simulated with a resolution of $5 \mu\text{m}$, while
 201 aggregates with $N_{mono} \geq 100$ are simulated with $10 \mu\text{m}$ resolution. With a resolution
 202 of $5 \mu\text{m}$ ($10 \mu\text{m}$) a plate monomer with $D_{max} = 3 \text{ mm}$ has a thickness of 4 (8) volume
 203 element layers. It should be noted that the sensitivity to resolution is smaller for monomer
 204 types with less extreme aspect ratios (e.g. columns).

205 The second major difference to previous aggregation studies using the model by
 206 Leinonen (2013) is that we extended the code in a way that we can also generate aggre-
 207 gates composed of monomers with different habits. The motivation for this new feature
 208 was based on observations that larger snowflakes often consist of a mixture of dendrites
 209 and needles (Lawson et al., 1998). The modified code allows the mixture of any num-
 210 ber of monomer types with any ratio of occurrence of the monomer types. Moreover, the
 211 settings (e.g. the truncation of the size distribution) can be set for each monomer type
 212 individually.

213 In order to account for a large variability of naturally observed particle shapes (Bailey
 214 & Hallett, 2009), we simulated a large suite of aggregates consisting of plates, columns,
 215 dendrites, needles and mixtures of dendrites and columns. The $m-D_{max}$ and $A-D_{max}$
 216 relations for the monomers are given in Table 1. Two sets of aggregates with mixed monomer

Table 1. Mass-size ($m(D_{max}, N_{mono} = 1) = a_{m,1} D_{max}^{b_{m,1}}$) and projected area-size ($A(D_{max}, N_{mono} = 1) = a_{A,1} D_{max}^{b_{A,1}}$) relationships for monomers ($N_{mono} = 1$) used in the aggregation model. All monomers have a grid resolution of $5 \mu m$.

Monomer type	$a_{m,1} [kgm^{-b_m}]$	$b_{m,1}$	$a_{A,1} [m^2m^{-b_A}]$	$b_{A,1}$
Plate	0.788	2.48	0.631	1.99
Dendrite	0.074	2.33	0.142	1.94
Column	0.046	2.07	0.008	1.54
Needle	0.005	1.89	0.002	1.42

Table 2. Grid resolution, size parameter λ^{-1} of the monomer distribution, and number of monomers N_{mono} used to create the aggregate dataset. D_{max} denotes the maximum size range of the generated aggregates in the dataset.

Resolution	λ^{-1}	N_{mono}	D_{max} of the aggregate
$5 \mu m$	$50 \mu m - 10 mm$	1,2,3,...,10,20,30,...,100	$\approx 1-2 cm$
$10 \mu m$	$50 \mu m - 10 mm$	200,300,...,1000	$\approx 3-5 cm$

217 types were created. For the first mixture, the selection of the monomer type is random
 218 with the same probability density function for both monomer types ("Mix1"). This would
 219 represent a scenario, where dendrites and needles coexist with similar PSD and likeli-
 220 hood of aggregation. For the second mixture, the monomers with $D_{max} < 1 mm$ are
 221 columns while dendrites are taken for larger monomers ("Mix2"). This choice is moti-
 222 vated by the fact that at temperature colder than $-20 \text{ }^\circ C$, the particle shape is more colum-
 223 nar while at temperatures between -20 and $-10 \text{ }^\circ C$ one finds more planar and dendritic
 224 crystals (Bailey & Hallett, 2009). Considering a thick cloud, we could assume that the
 225 small columnar crystals forming in the upper part of the cloud begin to form the first
 226 aggregate and then further grow by collection of larger dendrites at lower layers. Of course,
 227 both scenarios are quite ad-hoc and more detailed studies are needed to better under-
 228 stand the real properties of mixed-monomer aggregates. Our mixtures are thus rather
 229 intended to qualitatively analyze the differences of mixed monomer aggregates compared
 230 to single-monomer type aggregates.

231 The aggregation process strongly depends on the number concentration of parti-
 232 cles and their relative terminal velocity differences. It is therefore likely that aggrega-
 233 tion involves very different monomer sizes. In order to account for this variability, we
 234 vary λ^{-1} in a large range from 50 μm to 10 mm with 500 different values of λ^{-1} , spaced
 235 evenly in the logarithmic space. The monomer distribution is limited to sizes of 100 μm
 236 up to 3 mm following Leinonen and Moisseev (2015) in order to be consistent with the
 237 typical size range of observed ice particles. This limitation of the monomer size range
 238 leads to mean monomer sizes of the distribution ranging from 150 μm to 1.48 mm.

239 The spacing of the monomer number (Table 2) is finer at low N_{mono} and becomes
 240 more coarse at larger numbers. In this way, we can investigate the changes at small monomer
 241 numbers with greater detail. In fact, we expect the largest changes in snow properties
 242 at the transition from single monomers to aggregates composed of few pristine crystals.
 243 The coarser spacing of N_{mono} also limits computational costs. With our settings we ob-
 244 tain maximum aggregates sizes ranging from 3 cm to 5 cm which means that we include
 245 also the typically observed large snowflakes during intense snowfall on the ground (Lawson
 246 et al., 1998).

247 In Figure 2 several examples of similar sized aggregates simulated with different
 248 combinations of λ^{-1} , N_{mono} , and monomer types are shown. In total, 105'000 particles
 249 were simulated. Apart from the visual differences of shapes and structure, also the par-
 250 ticle properties such as mass, area, or terminal velocity show a wide range of values al-
 251 though all aggregates have maximum sizes ranging between 3 and 5 mm.

252 2.2 Hydrodynamic Models

253 Hydrodynamic models are needed in order to derive the terminal velocity v_{term} from
 254 the particle's mass m , projected area A and maximum size D_{max} . The most commonly
 255 used hydrodynamic models are Böhm (1992, hereafter B92), Khvorostyanov and Curry
 256 (2005, hereafter KC05) and Heymsfield et al. (2010, hereafter HW10). All models are
 257 based on particle boundary layer theory and rely on the Best number (X) approach (Abraham,
 258 1970). v_{term} is calculated via

$$v_{term} = \eta Re(X) / (\rho_a D_{max}) \quad (2)$$

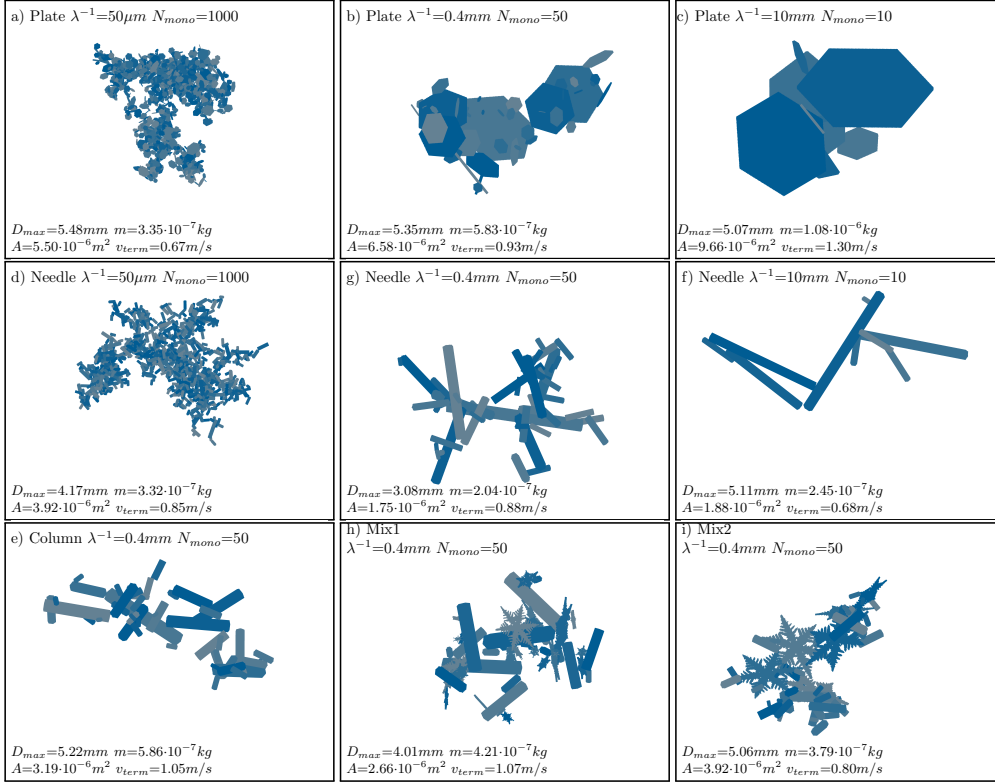


Figure 2. Examples of simulated aggregates with various monomer size parameters (λ^{-1}), number of monomers N_{mono} , and monomer types. All aggregates have a comparable maximum size (in the range between 3-5 mm). The terminal velocity v_{term} is calculated using the hydrodynamic model by Böhm (1992, see Section 2.2).

259 where η is the dynamic viscosity, Re the Reynolds number (parameterized as a function
260 of X) and ρ_a is the air density. X is defined as

$$X = C_d Re^2 \quad (3)$$

261 where C_d is the drag coefficient. The proportionality of X to the particle properties is
262 given by

$$X \sim m D_{max}^{0.5} A^{-0.25} \quad (4)$$

263 for B92.

264 For this study, we decided to use B92 because it best represents the saturation of
265 v_{term} for our simulated particles at larger aggregate sizes in accordance with observa-
266 tions (Figure 1). B92 includes an empirical correction of X due to wake turbulence which
267 reproduces the drag increase of large particles. X depends on the aspect ratio α , which
268 is larger than one for prolate and smaller than one for oblate particles. For this study,
269 we set α to 1.0, because aggregates with small values of N_{mono} are not easily classifiable
270 as either prolate or oblate and show in general a large variability of α .

271 To be able to interpret the dependency of v_{term} on N_{mono} in Section 4.3, we sketch
272 here how v_{term} scales with D_{max} in the simplified case of $Re \ll 1$ (Stokes drag) and
273 $Re \gg 1$ (Newtonian drag). For $Re \ll 1$, C_D is approximately proportional to $1/Re$.
274 Inserting this approximation and Equations 3 and 4 into Equation 2 yields:

$$v_{term} \sim m D_{max}^{-0.5} A^{-0.25} \quad (5)$$

275 If we approximate m and A by the power laws $m = a_m D_{max}^{b_m}$ and $A = a_A D_{max}^{b_A}$
276 we can express v_{term} solely as a function of D_{max} :

$$v_{term} \sim D_{max}^{b_m - 0.5 - 0.25b_A} \quad (6)$$

277 For $Re \gg 1$, C_D is approximately constant. In this case Equation 3 gives us $Re \sim$
278 $X^{0.5}$ and by using again the Equations (2 and 4) we get:

$$v_{term} \sim (m D_{max}^{-1.5} A^{-0.25})^{0.5} \sim (D_{max}^{b_m - 1.5 - 0.25b_A})^{0.5} \quad (7)$$

279 In both extreme cases of Re , v_{term} increases the faster with size the higher $b_m -$
280 $0.25b_A$ is and we expect this also to be in between these cases where Re transitions from

281 $Re \sim X$ to $Re \sim X^{0.5}$. This has certain implications for the dependency of v_{term} on
 282 N_{mono} (Section 4.3).

283 The differences between the three hydrodynamic models as well as an analysis of
 284 the potential impact of changing to different hydrodynamic models is discussed in the
 285 Appendix A2.

286 **3 Comparison of the Simulated Particle Properties to In-Situ Obser-** 287 **vations**

288 **3.1 Mass- and Area-Size Relations**

289 The particle properties m , A and D_{max} are used in hydrodynamic models to cal-
 290 culate v_{term} (Section 2.2). We evaluate relations of these particle properties and v_{term}
 291 with frequently used, in-situ measurements from Locatelli and Hobbs (1974, LH74) and
 292 Mitchell et al. (1990, M96). LH74 defined an equivalent diameter, that is equal to “the
 293 diameter of the smallest circle into which the aggregate as photographed will fit with-
 294 out changing its density”. M96 collected observations as a function of D_{max} without spec-
 295 ifying the exact definition. As a conversion of the diameter definition is not easily viable,
 296 we do not attempt to retrieve a diameter definition from the simulated particles, which
 297 is similar to the definitions used in these studies.

298 Except for the aggregates of dendrites, which have a considerably lower density than
 299 LH74 aggregates of dendrites, the absolute value of m of the simulated aggregates is sim-
 300 ilar to the observations, where the same monomer type is available (Figure 3). The slope
 301 of the $m - D_{max}$ relation from this study is comparable to the slope from M96, while
 302 LH74 report lower slopes for the aggregates of dendrites. The $m - D_{max}$ relation of the
 303 mixed aggregates (“Aggregates of unrimed radiating assemblages of plates, side planes,
 304 bullets, and columns”, LH74 mix), however, has a similar slope to the simulated Mix2
 305 aggregates. The mixS3 and sideplane aggregates from M96 are similar to many simu-
 306 lated aggregates (composed of different monomers).

307 M96 derived $A - D_{max}$ relations for “assemblages of planar polycrystals in cirrus
 308 clouds” (M96 polycrystal in Figure 3) based on observations in a relatively small size range
 309 and applied them to other aggregate types. This $A - D_{max}$ relation is also used in sev-
 310 eral microphysics schemes (Morrison & Milbrandt, 2015; Brdar & Seifert, 2018). The ab-
 311 solute value of A given in M96 is slightly higher than A of the simulated particles from

312 this study (except for the aggregates of plates). The slope of the $A - D_{max}$ relations
 313 is slightly higher ($b_A = 1.88$) in M96 observations compared to the relations from this
 314 study ($1.79 < b_A < 1.88$). Observations of aggregates composed of the same monomer
 315 types than the one used in these studies are not available.

316 **3.2 Terminal Velocity-Size Relations**

317 Observations of v_{term} vs. size have been reported using several different definitions
 318 of the diameter (Szyrmer & Zawadzki, 2010). To facilitate a consistent comparison be-
 319 tween the observations from the PIP instrument (which are described in Section A1) and
 320 v_{term} of the simulated aggregates, we use similar bin sizes and a consistent diameter def-
 321 inition, which is the maximum dimension from a side projection ($D_{max,side}$; Figure 3c,d).
 322 Displayed are the median and the 25 and 75 percentiles of v_{term} of the detected parti-
 323 cles. Bins with fewer than 1000 particles are excluded from the statistics. Although LH74,
 324 M96 and Kajikawa (1972, K73) did not use the same definition as the PIP-CARE dataset,
 325 fits from this study are also shown in Figure 3c and d because they can ease the com-
 326 parison with other studies.

327 At small sizes ($D_{max} < 1$ mm), v_{term} of the simulated aggregates of dendrites is
 328 close to v_{term} of the monomers from Kajikawa (1972, K73, Figure 3c). The plate monomers
 329 in K73 are reported with a similar v_{term} as the aggregates of plates, needles and Mix1
 330 (which all have similar values). Note that v_{term} of plates and dendrites from K73 and
 331 v_{term} of all aggregates simulated in this study (except for the aggregates of columns and
 332 "Mix2") are considerably smaller than v_{term} of the aggregates from the PIP-CARE dataset
 333 and LH74. The observations from LH74 are within the 25th and 75th percentile of the
 334 PIP-CARE dataset. The median of v_{term} of the simulated aggregates of this study in-
 335 creases faster with size compared to the in-situ observations at sizes of several mm (Fig-
 336 ure 3d). Only v_{term} of the mixture of small columns and large dendrites ("Mix2") have
 337 a comparably low slope. Potential reasons for this mismatch are limitations of the ob-
 338 servations at these sizes (Brandes et al., 2008), turbulence affecting the observations (Garrett
 339 & Yuter, 2014b), missing processes in the aggregation model (e.g. depositional growth
 340 on aggregates) or the dominance of monomer type mixtures in the aggregates.

341 Figures 3c and d also show v_{term} calculated with B92 and the $m - D_{max}$ and $A -$
 342 D_{max} relations from M96 (which did not measure v_{term} directly). The simulated slope

343 of v_{term} from M96 observed aggregates is similar to the one simulated in this study while
 344 the absolute value is slightly higher.

345 At sizes larger than about 5 mm, the simulated and the observed v_{term} reach a sat-
 346 uration value close to 1 m s⁻¹. The median of v_{term} of most simulated aggregates lies
 347 within the 25th and 75th percentile in the sub-cm range, except the aggregates with the
 348 most extreme density (aggregate of dendrites and aggregates of columns). Thus, based
 349 on this comparison, these aggregates can be considered most representative for many ag-
 350 gregates found in the atmosphere.

351 4 Parameterization of Particle Properties

352 The relationships between hydrometeor properties such as mass, size, projected area,
 353 and velocity are key components in any ice microphysics scheme and they strongly in-
 354 fluence various microphysical processes (e.g., sedimentation, depositional growth, aggre-
 355 gation, or riming). Different microphysics schemes require a more or less simplified pa-
 356 rameterization of particle properties. To address these different needs, we derive in this
 357 section fits for m and A as a function of D_{max} and N_{mono} that can be used in micro-
 358 physics schemes, which can predict m and N_{mono} given a certain D_{max} (Section 4.2).
 359 Of course, most bulk schemes require less detailed fits and hence we also derive fits of
 360 m , A , and v_{term} as a function of D_{max} or the mass-equivalent diameter D_{eq} . This also
 361 allows us to assess the potential error of the less detailed fits (Section 4.5) while their
 362 impact on modeled processes is studied later in Section 5.

363 4.1 Fitting Approach for Monomer Number Dependent Particle Prop- 364 erties

365 The particle properties of the monomers are reported in Table 1. The subsequent
 366 aggregation process determines how the particle properties will change with increasing
 367 N_{mono} . As we are particularly interested in quantifying how key particle properties such
 368 as m and A change during the aggregation process, we normalize the aggregate prop-
 369 erties by the property of a monomer with the same D_{max}

$$f_p(D_{max}, N_{mono}) = \frac{p(D_{max}, N_{mono})}{p(D_{max}, N_{mono} = 1)}. \quad (8)$$

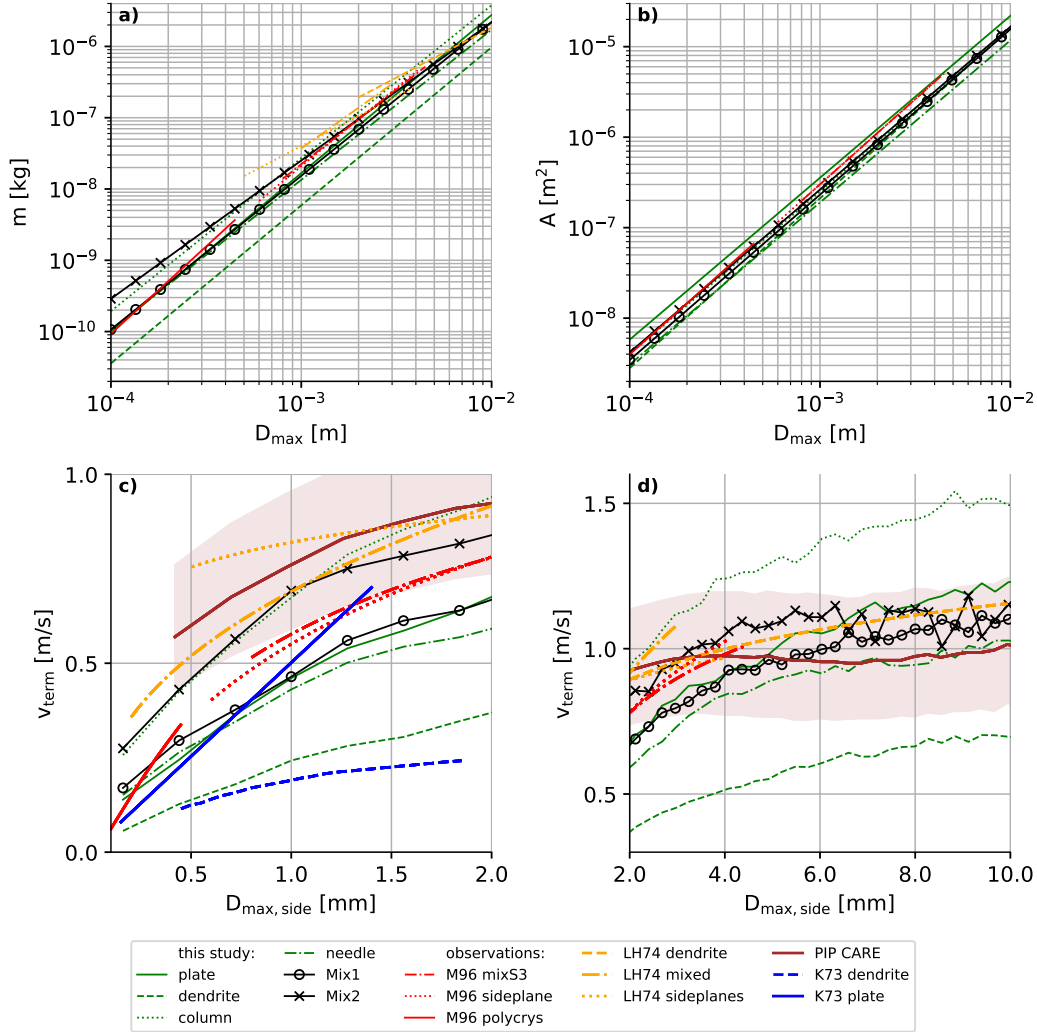


Figure 3. Particle properties of simulated aggregates from this study (green and black), from previous studies (Mitchell et al., 1990; Locatelli & Hobbs, 1974; Kajikawa, 1972)[M96,LH74, K73] and measurements of ice particle observed by PIP at the CARE site (brown, see text). a) m vs. D_{max} ; b) A vs. D_{max} ; c) median (and 25th and 75th percentile for PIP CARE) of v_{term} vs. side projected maximum dimension $D_{max,side}$ for data from this study and vs. the size definition of the respective study (v_{term} is directly observed in K73 and LH74 and calculated with B92 from the $m - D_{max}$ and $A - D_{max}$ relations of M96) d) same as c) but for larger sizes. Note that K73 observations are for single monomers.

Table 3. Coefficients in the normalizing functions f_m and f_A (notation as in Equation 9) for different monomer types.

Monomer type	$a_{f,m}$	$a'_{f,m}$	$b_{f,m}$	$b'_{f,m}$	$a_{f,A}$	$a'_{f,A}$	$b_{f,A}$	$b'_{f,A}$
Plate	-0.673	0.364	-0.092	0.091	-0.473	0.322	-0.021	-0.166
Needle	0.162	-0.008	0.018	0.102	0.349	0.005	0.060	0.013
Dendrite	-0.288	0.215	-0.042	-0.056	-0.100	0.131	-0.019	-0.059
Column	0.079	-0.006	0.033	0.086	0.273	0.025	0.058	0.034

370 p represents the particle properties (mass or area), $p(D_{max}, N_{mono} = 1)$ is the prop-
 371 erty of single monomers, and f_p is the normalizing function. A normalizing function which
 372 is larger (smaller) than 1 indicates that the aggregate properties are larger (smaller) than
 373 its composing monomer with the same size (Figure 4).

374 To fit f_p to various monomer types, we use a combination of rational functions sim-
 375 ilar to the approach presented in Frick et al. (2013)

$$f_p(D_{max}, N_{mono}) = 10^{\frac{a_{f,p} \log_{10}(N_{mono})}{1+a'_{f,p} \log_{10}(N_{mono})}} D^{\frac{b_{f,p} \log_{10}(N_{mono})}{1+b'_{f,p} \log_{10}(N_{mono})}}. \quad (9)$$

376 The coefficients of f_p for all monomer types can be found in Table 3. Note, that we ex-
 377 cluded the mixture of monomer types from the monomer dependent analysis because our
 378 normalization approach cannot be applied to monomer mixtures.

379 4.2 Dependence of Aggregate Mass and Area on Monomer Number

380 Motivated by the common classification of unrimed ice hydrometeors in cloud ice
 381 and snow in many bulk schemes, we will investigate in this section how mass and area
 382 change when building up an aggregate with an increasing number of monomers. In par-
 383 ticular, we want to explore whether the properties change smoothly with monomer num-
 384 ber or whether they show any sharp transition at certain monomer numbers.

385 When we compare the mass of an aggregate with the mass of its monomer of the
 386 same size, we find in some conditions the aggregate to be heavier or lighter than the monomer.
 387 The relevant mechanisms which explain this behavior are illustrated in Figure 4 for ag-
 388 gregates of plates. Note that we assume for simplicity a monodisperse monomer distri-

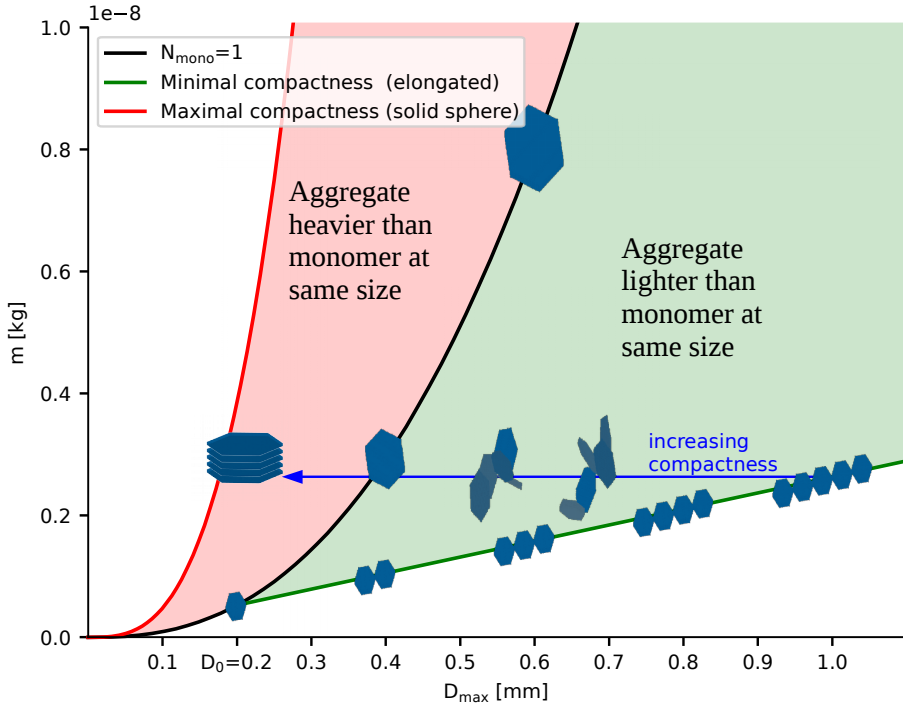


Figure 4. Schematic illustration of how compactness of aggregates can cause them to be heavier or lighter compared to a monomer of the same size. For simplicity a monodisperse monomer size distribution with monomer sizes of $D_{max}=0.2$ mm is used. The red line indicates the maximum theoretical compactness of mass of an ice sphere. The black lines shows the $m - D_{max}$ relation of the monomer (plate). The green line represents the $m - D_{max}$ relation of the least compact configuration of the plate monomers in an aggregate by aligning the plates along their maximum dimension. Particles have lower mass ($f_m < 1$) in the green shaded area and larger mass ($f_m > 1$) in the red shaded region compared to an equal-size plate.

389 bution in Figure 4. When we consider pure depositional growth, we obtain a specific m –
390 D_{max} relation for each monomer type (Table 1; black line in Figure 4). One extreme ag-
391 gregation scenario, which leads to the maximal size of an aggregate with a given num-
392 ber of monomers (which in this simplified case of a monodisperse distribution also de-
393 termines its mass) would be if we assume that all monomers align along their maximum
394 dimension. Clearly, the resulting aggregate would have a smaller m than a monomer of
395 the same size. Of course, this maximal elongated assemblage of monomers is rather un-
396 likely and thus the aggregate will have a more compact structure. If we imagine rear-
397 ranging the monomers inside the aggregate in a progressively more packed configuration
398 (indicated by the horizontal arrow in Figure 4), we might be able to reach the point where
399 the size of the aggregate equals the one of the equal-mass monomer. At this point, it might
400 be even possible to pack the monomers in a way that their size is smaller than an equal-
401 mass monomer. A simple example of such an extreme packing would be to stack a num-
402 ber of plates on top of each other, i.e. along their smallest axis. Whether an aggregate
403 can be smaller than an equal-mass monomer is of course also dependent on how close
404 the monomer $m - D_{max}$ relation is to the theoretical maximum packing of an equal-
405 mass sphere.

406 The dependency of A on N_{mono} can be understood analogously. Also for A , the
407 maximal elongated assemblage of the monomers leads to a lower A of the aggregate com-
408 pared to the monomer of the same size, but in reality, the monomers will assemble in a
409 more compact way. In addition, we have to consider that A is not simply additive as it
410 is the case for m . Overlap (in the horizontally projected plane) and non-horizontal align-
411 ment of the constituting monomers lead to a smaller A than the sum of A of the con-
412 stituting monomers. Based on these simplified considerations it becomes clear that the
413 dependency of m and A on N_{mono} is determined by the exponent of the monomer power
414 laws and the overall “compactness” of the aggregates.

415 When considering the monomer dependence of all simulated aggregates, we find
416 the most different behavior for plate and needle aggregates. For plate aggregates, m and
417 A steadily decrease with an increasing number of monomers (Figure 5b,d). From the prin-
418 cipal considerations discussed in Figure 4, this behavior can be well understood. The plate
419 monomers have the largest exponent ($b_{m,1} = 2.48$) of all monomers (Table 1) while the
420 monomers itself show relatively loose connections within the aggregate (Figure 2a-c). In-
421 terestingly, the aggregate mass for very small N_{mono} can be slightly larger than the equal-

size monomer while A is immediately decreasing for $N_{mono} > 1$. This effect can be easily understood when considering, for example, two plates that connect in a 90° angle of their major axes.

An opposite behavior is found for needle aggregates (Figure 6b,d). With increasing N_{mono} , both m and A of the aggregates become larger than the equal-size monomers. In contrast to plates, the needle monomers have the lowest exponents for the m and A power laws (Table 1). The aggregates of the more one-dimensional needles also show a more compact packing.

Dendrite and column aggregates have been analyzed similarly (according figures can be found in Supplement). The dendrites are similar to plates, while the columns are similar to needles. However, for all aggregate types, we find a relatively smooth transition of m and A when changing from single monomers to aggregates. For these two particle properties, we are unable to identify a “jump” due to the onset of aggregation. The next sections will show whether this behavior will change when deriving terminal velocity from m and A .

4.3 Dependence of Terminal Velocity on Monomer Number

The terminal velocity for all aggregates was calculated with the hydrodynamic model of B92 (Section 2.2). In Figure 7a, v_{term} is shown as a function of D_{max} for plate aggregates. Note, that the fits have been derived by applying B92 to the $m-D_{max}$ and $A-D_{max}$ fits rather than fitting them directly to the cloud of individual v_{term} . In this way, we are consistent with the way how v_{term} relations are usually connected to $m-D_{max}$ in bulk schemes. The terminal velocity of plate aggregates steadily decreases with increasing N_{mono} . This dependency is much less pronounced at small D_{max} as compared to the largest sizes. However, it should be noted that the fits for very small monomer numbers are probably unrealistic for large D_{max} as we do not expect aggregates of cm sizes to be composed of only a few large plates. In fact, the here used geometrical relations for the plate monomers are only valid for a maximum size of 3 mm (Pruppacher & Klett, 2010).

We find a similar decreasing v_{term} with increasing N_{mono} for dendrites (see Supplement). As we might expect from the different change of m and A with N_{mono} seen in Figure 7a, also the behavior of v_{term} with increasing N_{mono} is different for needles (Fig-

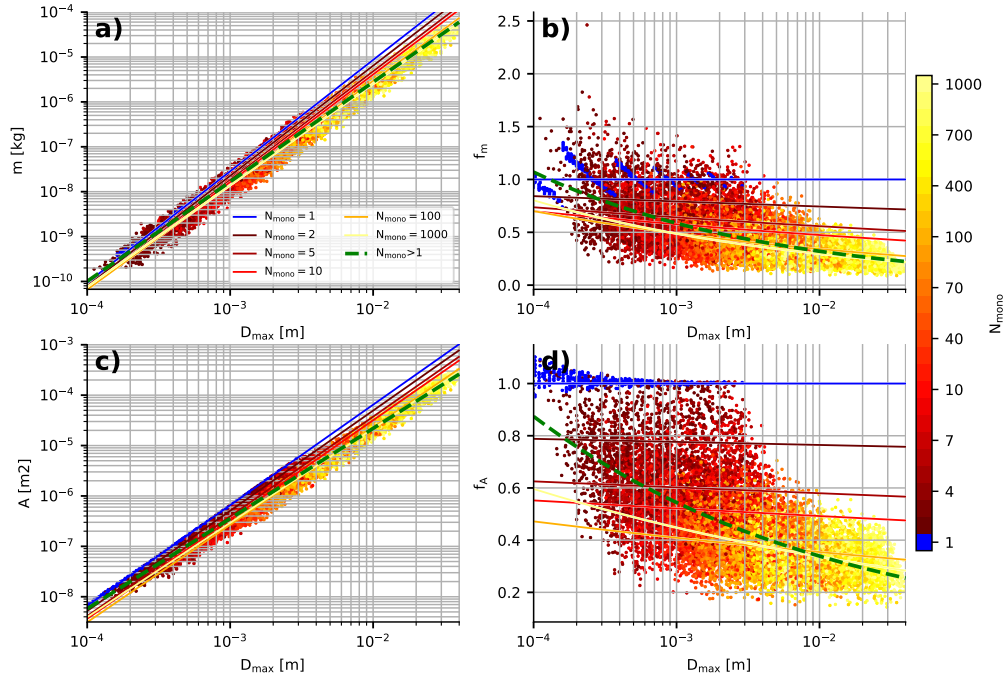


Figure 5. (a, c) m and A of the simulated plate aggregates as a function of D_{max} . (b, d) The normalizing functions f_m and f_A (defined in Equation 8) quantify the deviation of the aggregates' m or A from a monomer with same D_{max} . The dots indicate the properties of individual particles with the color showing N_{mono} . Lines indicate m and A for constant N_{mono} as a result of the monomer number dependent fits and for all aggregates ($N_{mono} > 1$).

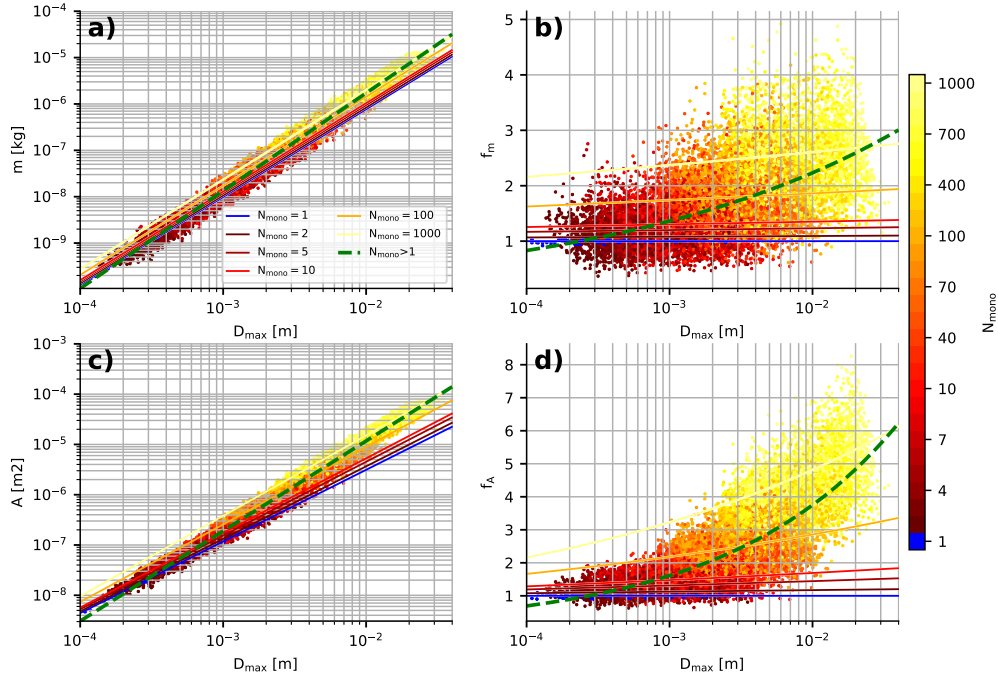


Figure 6. Same as Figure 5 but for aggregates of needles.

453 ure 7). Needles aggregates seem to fall slightly faster when their monomer number in-
 454 creases. Interestingly, all aggregates reveal a very low dependence of v_{term} on monomer
 455 number at small sizes which is in contrast to assumptions in some microphysics schemes
 456 (Figure 1). Besides, all aggregates reveal a saturation of v_{term} at large (centimeter) sizes
 457 which is in good agreement with observations (Figure 1). However, the absolute value
 458 of the saturation v_{term} ranges from 0.8 to 1.6 m s⁻¹ depending on the monomer type.

459 Because v_{term} of monomers and aggregates is converging towards the same value
 460 at small sizes (Figure 7), we can use the previously derived scaling relation (Equations
 461 6 and 7) to relate the dependency of v_{term} on N_{mono} to the exponents b_m and b_A in the
 462 $m-D_{max}$ relation. Starting from a similar value of v_{term} at small sizes, v_{term} of an av-
 463 erage aggregate increases slower than v_{term} of a monomer if $s_{monodep} = b_{m,agg} - b_{m,1} -$
 464 $0.25(b_{A,agg} - b_{A,1}) < 0$ (cf. 6 and 7). As a result, at larger sizes, v_{term} of the aggregate
 465 is lower than v_{term} of the monomer. In an analog way, v_{term} of an aggregate is larger
 466 than v_{term} of the monomer if $s_{monodep} > 0$. As $b_{m,agg}$ and $b_{A,agg}$ is similar for all ag-

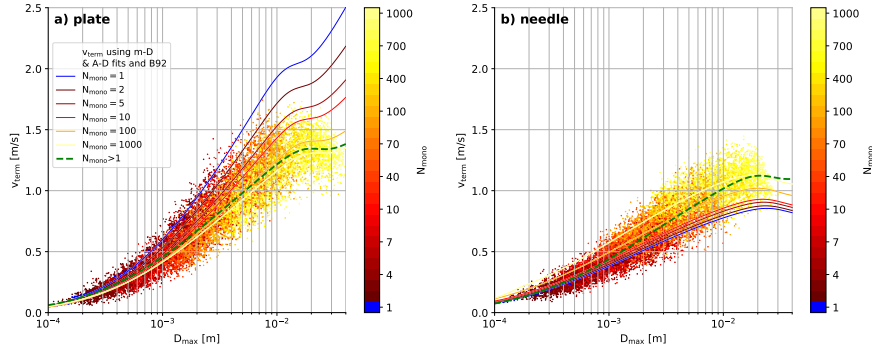


Figure 7. v_{term} vs. D_{max} for the simulated aggregates of plates and needles. The dots indicate the properties of individual particles with the color showing N_{mono} . Lines indicate v_{term} for constant N_{mono} as a result of the monomer number dependent fits and for all aggregates ($N_{mono} > 1$). Note that the fits have been derived by applying B92 to the $m - D_{max}$ and $A - D_{max}$ (Table 3) fits rather than fitting them directly to the cloud of individual v_{term} .

gregates (Table 4), the sign of v_{term} with increasing N_{mono} depends mainly on $b_{m,1}$ and $b_{A,1}$. For plates and needles $s_{monodep}$ equals -0.21 and 0.12 , respectively.

How the particle properties change with increasing N_{mono} as well as the absolute values of calculated v_{term} depends on the choice of the hydrodynamic model. Finding the optimal formulation of hydrodynamic models for ice and snow particles is still an active field of research (Westbrook & Sephton, 2017; Nettesheim & Wang, 2018) and outside the scope of this study. In Appendix A2, we tested the sensitivity of the results to the choice of the hydrodynamic model for plate aggregates. HW10 seems to yield overall similar results to B92 except for the saturation at large diameters. For KC05, the monomer dependence is much weaker. However, all hydrodynamic models show an overall small monomer dependence at small particle sizes.

It has also been observed (e.g. Garrett & Yuter, 2014a) that tumbling of particles caused for example by turbulence might decrease the effective projected area and therefore increase v_{term} . We also tested the sensitivity of our results to different degrees of tumbling (Section A22). As expected, the effect of tumbling is largest for single crystals (due to their more extreme aspect ratio) but strongly decreases for aggregates. Certainly, for aggregates, the choice of the hydrodynamic model has a larger effect of v_{term} than different assumptions on particle tumbling.

Table 4. Mass-size ($m(D_{max}) = a_{m,agg} D_{max}^{b_{m,agg}}$) and projected area-size ($A(D_{max}) = a_{A,agg} D_{max}^{b_{A,agg}}$) relationships for aggregates ($N_{mono} > 1$) in the aggregate model.

monomer type	$a_{m,agg}$ [kgm^{-b_m}]	$b_{m,agg}$	$a_{A,agg}$ [$m^2m^{-b_A}$]	$b_{A,agg}$
Plate	0.076	2.22	0.083	1.79
Needle	0.028	2.11	0.045	1.79
Dendrite	0.027	2.22	0.090	1.88
Column	0.074	2.15	0.060	1.79
Mix1	0.045	2.16	0.070	1.83
Mix2	0.017	1.95	0.066	1.79

4.4 Mean Particle Properties of Monomers and Aggregates of Different Monomer Types

The relatively continuous change of particle properties with N_{mono} found in the last section justifies a simplified fit, which is also necessary for implementing the results into common bulk microphysics schemes. These schemes often only contain two classes for unrimed ice particles, usually denoted as cloud ice (monomers) and snow (aggregates).

Figure 8a, b shows the derived $m-D_{max}$ relations for single monomers ($N_{mono} = 1$) and the derived v_{term} based on the $m-D_{max}$ and $A-D_{max}$ relations summarized in Table 1. Similar fits of m and v_{term} to aggregates of any monomer number large than 1 are shown in Figure 8c, d; the fit coefficients can be found in Table 4.

The $m-D_{max}$ relations for monomers show a larger spread especially for larger sizes as compared to the aggregates. This is expected considering that the exponents for monomers range between 1.89 to 2.48 (Table 1) while the exponents for aggregates are between 1.95 and 2.22 (Table 4). The values for aggregates agree well with theoretical aggregation studies (Westbrook et al., 2004b) as well as in-situ observations (Section 3.1). Despite the similar exponent, the effective density of the aggregates varies considerably (compare m at a given size in Figure 8c). Aggregates of columns exhibit the highest density, while aggregates of dendrites show the lowest density, which is in agreement with Hashino and Tripoli (2011).

504 The differences in the $m-D_{max}$ relation are linked to the resulting $v_{term}-D_{max}$
 505 relation (Figure 8c, d). At $D_{max} = 5$ mm, the v_{term} of different monomers spread nearly
 506 1 m s^{-1} . The differences are in general smaller for aggregates. Interestingly, most ag-
 507 gregate types reveal very similar v_{term} . The main exceptions are dendrite aggregates with
 508 the slowest, and column aggregates with the fastest v_{term} . v_{term} of the Mix2 aggregates
 509 increases slower with increasing D_{max} compared to the other aggregates.

510 Similar to the previous monomer number dependent fits, also the “two-category”
 511 fits show similar v_{term} at small sizes. The monomer type appears to have in general a
 512 much larger impact on v_{term} than the classification into certain N_{mono} regimes.

513 4.5 Power-Law and Atlas-type Fits for Terminal Velocity

514 Power-law fits for m , A , and v_{term} are commonly used in bulk schemes. Especially
 515 for v_{term} , the power law introduces inconsistencies with observations because a satur-
 516 ation value for v_{term} as observed for raindrops or snowflakes cannot be represented. In-
 517 stead of using standard power laws in the form

$$v(D_{max}) = a_{vD_{max}} D^{b_{vD_{max}}} \quad (10)$$

518 and the two fit parameters $a_{vD_{max}}$ and $b_{vD_{max}}$, Atlas et al. (1973) proposed a three-
 519 parameter ($\alpha_{D_{eq}}$, $\beta_{D_{eq}}$, $\gamma_{D_{eq}}$) formulation

$$v_{term}(D_{eq}) = \alpha_{D_{eq}} - \beta_{D_{eq}} \exp(-\gamma_{D_{eq}} D_{eq}). \quad (11)$$

520 Formulating this “Atlas-type” fit with the mass equivalent diameter D_{eq} instead of D_{max}
 521 has been found to provide optimal fit quality for snow aggregates (Seifert et al., 2014).
 522 For small (large) values of D_{eq} , v_{term} approaches $\alpha_{D_{eq}} - \beta_{D_{eq}}$ ($\alpha_{D_{eq}}$). With increasing
 523 values of γ , the transition from small to larger values of v_{term} is shifted towards larger
 524 values of D_{eq} . Approximations for bulk collision rates based on Atlas-type fits can be
 525 found in Seifert et al. (2014) which makes them usable in bulk microphysics schemes with-
 526 out the necessity of look-up tables.

527 Power-law and Atlas-type relations have been applied to the various aggregates and
 528 the fit coefficients are summarized in Table 5. For the fitting, we did not use v_{term} of
 529 the individual particles but directly applied to fit to v_{term} derived with B92 and the ex-
 530 isting $m - D_{max}$ and $A - D_{max}$ relations.

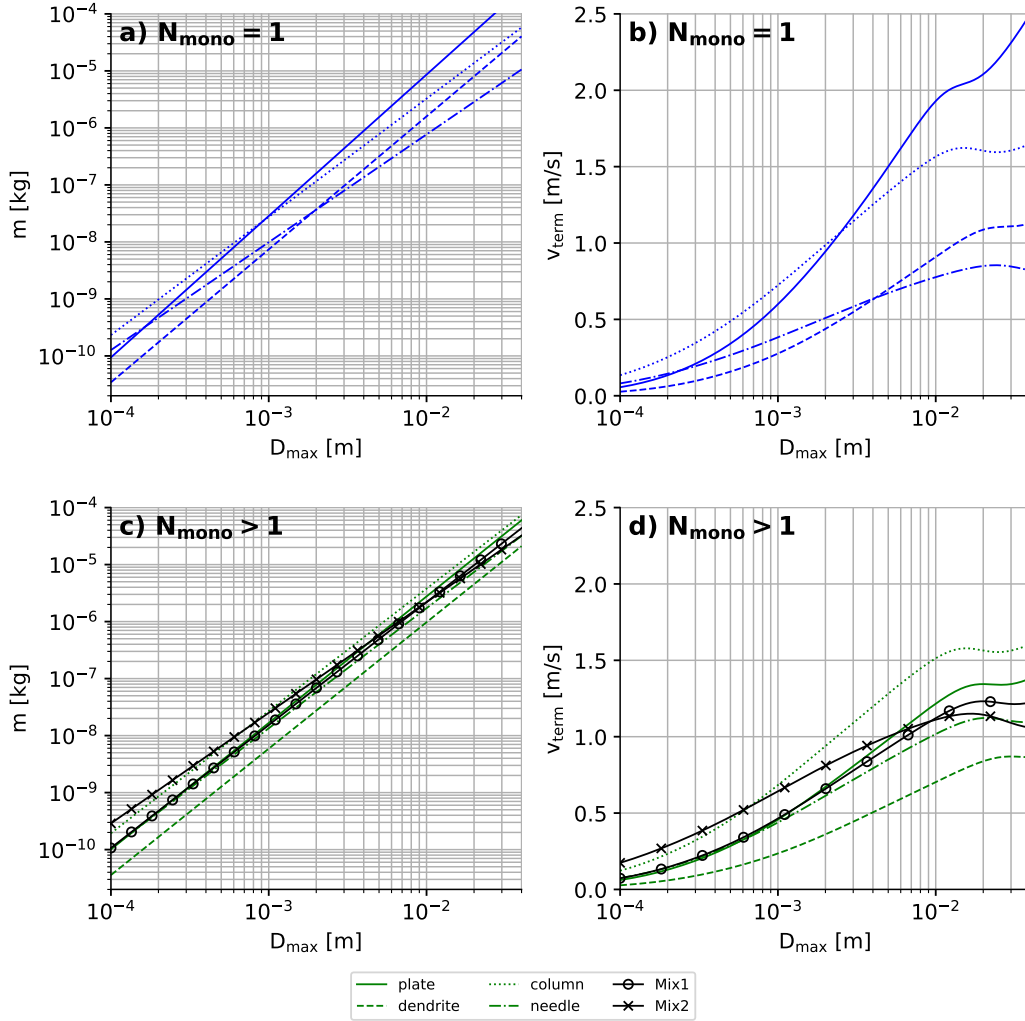


Figure 8. Particle m (a, c) and v_{term} (b, d) as a function of D_{max} calculated with B92 using the derived $m/A - D_{max}$ relations (Table 1 and 4). Particles are separated into single monomers (a, b) and aggregates (c, d) composed of various monomer types (see legend).

531 In Figure 9 the different fits are exemplary compared for plate monomers and their
 532 aggregates. Note that the saturation region ($D_{max} > 1$ cm) has been excluded for the
 533 power-law fits. It can be seen in Figure 9b that the Atlas-type fit is very close to the the-
 534oretical line calculated with B92 and the $m-D_{max}$ and $A-D_{max}$ relations. The power-
 535law fits (Figure 9a) provide only a close fit to the theoretical values at the smaller size
 536range. Between 300 μm and 4 mm they cause a slight underestimation while at larger
 537sizes they increasingly overestimate v_{term} . Similar fits have been derived for all aggre-
 538gate types (Table 5, figures for other monomer types similar to Figure 9 can be found
 539in the supplemental material).

540 When we compare the calculated v_{term} with some widely used microphysics schemes
 541 (Figure 9c) we find most schemes to overestimate v_{term} at small sizes (except of the cloud
 542ice category in Morrison et al. (2005)). The absolute values for v_{term} at small sizes are
 543strongly dependent on monomer type and hence, additional constraints should be pro-
 544vided by additional observations. However, the aggregation model shows independent
 545on the monomer type that at sub-mm sizes there should be no strong “jump” in v_{term}
 546between ice particles and small aggregates. Also in the cm-size range, models using a
 547power-law formulation are strongly overestimating v_{term} for all aggregate types.

548 **5 Application and Sensitivity Tests in the Lagrangian Particle Model** 549 **McSnow**

550 In this section, we will test the possible impact of implementing particle proper-
 551ties with different amount of complexity (monomer number dependence) or different fit-
 552ting functions (power law vs Atlas type) on the simulation of sedimentation, aggrega-
 553tion and depositional growth. For this, we use a one-dimensional setup of the Lagrangian
 554particle model McSnow (Brdar & Seifert, 2018), which provides the flexibility to imple-
 555ment the different particle property formulations.

556 For simplicity, only sedimentation, depositional growth and aggregation are con-
 557sidered in our simulations. Aggregation is calculated with a Monte-Carlo algorithm fol-
 558lowing Shima et al. (2009) and the sticking efficiency of Connolly et al. (2012) is used.
 559McSnow is based on the Lagrangian super-particle approach (Shima et al., 2009), which
 560allows deriving not only the particle mass and its multiplicity X , but it also predicts the
 561number of monomers the particle is composed of. This information is key to test the N_{mono}
 562dependent particle relations. The thermodynamic profiles and the overall setup is sim-

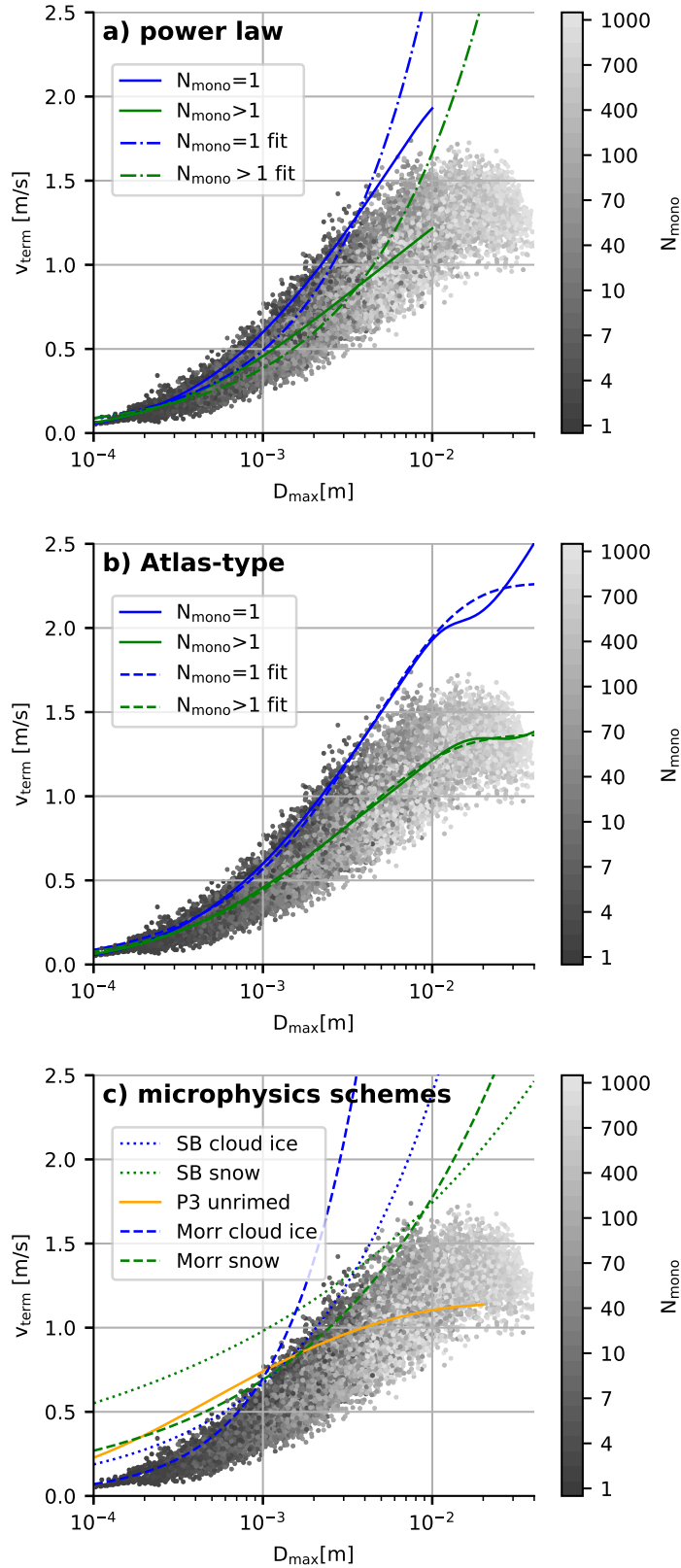


Figure 9. v_{term} of individual plate aggregates (gray scale, a-c) and v_{term} derived with B92 and the $m/A - D_{\text{max}}$ of plate monomers (Table 1, solid blue line in a and b) and aggregates (Table 4, solid green line in a and b). Power-law (dashed-dotted, a) and Atlas-type fits (dashed-dotted, b) have been applied to the directly calculated v_{term} (solid lines) rather than the individ-

Table 5. Derived coefficients of the power-law and Atlas-type fits (Equations 10 and 11) for monomers and aggregates of different monomer types.

Monomer type	$\alpha_{D_{eq}}$ [m/s]	$\beta_{D_{eq}}$ [m/s]	$\gamma_{D_{eq}}$ [1/m]	$a_{v,D_{max}}$ [$\text{m}^{1-b_{v,D_{max}}}$ /s]	$b_{v,D_{max}}$
$N_{mono} = 1$					
Plate	2.265	2.275	771.138	90.386	0.755
Needle	0.848	0.871	2276.977	9.229	0.481
Dendrite	1.133	1.153	1177.000	41.870	0.755
Column	1.629	1.667	1585.956	22.800	0.521
$N_{mono} > 1$					
Plate	1.366	1.391	1285.591	30.966	0.635
Needle	1.118	1.133	1659.461	17.583	0.557
Dendrite	0.880	0.895	1392.959	24.348	0.698
Column	1.583	1.600	1491.168	23.416	0.534
Mix1	1.233	1.250	1509.549	21.739	0.580
Mix2	1.121	1.119	2292.233	8.567	0.393

563 ilar to previous simulation studies with McSnow in Brdar and Seifert (2018) and Seifert
564 et al. (2019). Particles are initialized at the upper boundary of the 5km thick domain
565 with a mass flux of $F_m = 2 \cdot 10^{-5} \text{ kg s}^{-1}$ and a mean mass of the particle size distri-
566 bution of $m_{mean} = 2 \cdot 10^{-10} \text{ kg}$. The initial ice particles follow a generalized gamma dis-
567 tribution of particle mass with a shape parameter of 0 and a dispersion parameter of 1/3
568 (following Equation 9 in Khain et al. (2015)). The temperature decreases linearly from
569 273.1 K at $z=0 \text{ km}$ to 242.2 K at $z = 5 \text{ km}$. The supersaturation over ice is held con-
570 stant at 5 % with respect to ice in the whole column and is not consumed by the growth
571 of the particle. The simulations are performed with 250 vertical levels, which results in
572 a vertical resolution of 20 m. The model time step is set to 5 s and the initial multiplic-
573 ity is chosen to be 1000. The simulations are run for 10h, from which the last 5h are av-
574 eraged in 10 min intervals to reduce noise in the analyzed profiles.

575 In the following, we will focus the comparison on particle number flux (F_N), mass
576 flux (F_M), and mean mass m_{mean} (which is the ratio between the integrated mass den-
577 sity q_m and the integrated number density q_N).

Table 6. Settings of the McSnow control (CTRL) and sensitivity runs. The second column specifies the monomer type from which the $m - D_{max}$ and $A - D_{max}$ (and $v_{term} - D_{max}$ for the Atlas and power law run) fit is taken. The third column denotes how the N_{mono} dependency is represented. $f_p(N_{mono}, D_{max})$ is the normalizing function with full N_{mono} dependence (Section 4.1), $f_p(N_{mono} = 1; N_{mono} > 1, D_{max})$ denotes only a binary separation in $N_{mono} = 1$ and $N_{mono} > 1$, and $f_p = f(N_{mono} > 1, D_{max})$ indicates that the fit for all aggregates $N_{mono} > 1$ is taken for all particles (Section 4.4). The fourth column indicates whether v_{term} is calculated using B92 or with a parameterized relation of $v_{term} - D_{max}$ (Section 4.5). The fifth column shows the precipitation rate ($F_m(z = 0m)$) and in brackets its deviation from the CTRL run. The last column lists the mean mass m_{mean} at the surface, and the ratio of m_{mean} between the simulation and its CTRL run (in brackets).

Simulation	Habit	$m - D_{max}/A - D_{max}$ relations	$v_{term} - D_{max}$ relations	precipitation rate [mm/h] (difference to CTRL)	$m_{mean,sens}$ [μg] ($m_{mean,sens}/$ $m_{mean,CTRL}$)
<i>in Figure 10</i>					
CTRL	Plate	$f_p(N_{mono}, D_{max})$	B92	1.844	4.214
	/monodep				
Binary	Plate	$f_p(N_{mono} = 1;$ $N_{mono} > 1, D_{max})$	B92	1.763 (-4.4%)	5.241 (1.2)
Constant	Plate	$f_p(N_{mono} > 1, D_{max})$	B92	1.833 (-0.6%)	5.789 (1.4)
<i>in Figure 12</i>					
Atlas	Plate	$f_p(N_{mono} = 1;$ $N_{mono} > 1, D_{max})$	Atlas type	1.881 (+2.0%)	4.424 (x1.0)
Powerlaw	Plate	$f_p(N_{mono} = 1;$ $N_{mono} > 1, D_{max})$	Power law	1.761 (-4.5%)	21.013 (x5.0)
<i>in Figure 11</i>					
Needle CTRL	Needle	$f_p(N_{mono}, D_{max})$	B92	1.988	13.173
	/monodep				
Needle					
Binary	Needle	$f_p(N_{mono} = 1;$ $N_{mono} > 1, D_{max})$	B92	2.019 (+1.6%)	10.443 (0.8)
Needle					
Constant	Needle	$f_p = f(N_{mono} > 1, D_{max})$	B92	2.038 (+2.5%)	10.390 (0.8)

578 In the first simulation experiment shown in Figure 10, we include particle proper-
 579 ties for which the full N_{mono} dependence is taken into account (Table 5). This setup we
 580 call hereafter the control simulation (CTRL). Profiles are separated into single monomers
 581 ($N_{mono} = 1$) and aggregates ($N_{mono} > 1$) to better distinguish the effects on what
 582 we might define as “cloud ice” and “snow” category in a bulk scheme. This separation
 583 might be important considering that there can be cases of weak aggregation. With weak
 584 aggregation, most of the particles will remain monomers and thus it is especially impor-
 585 tant to match profiles of these particles accurately.

586 In general, aggregation decreases the number flux (F_N), while the increase in the
 587 mass flux (F_m) is due to depositional growth. The mass flux of aggregates increases also
 588 due to conversion from monomers to aggregates by aggregation. The combination of both
 589 processes is causing m_{mean} to continuously increase towards the surface. Aggregation
 590 rates in McSnow are proportional to the gravitational collection kernel (Equation 21 in
 591 Brdar and Seifert (2018)). Thus, the probability of collision for two particles is high if
 592 they have strongly different v_{term} and if the sum of their cross-sectional areas is large.
 593 F_N of the monomers ($N_{mono} = 1$) decreases monotonously with decreasing height be-
 594 cause the monomers are converted into aggregates ($N_{mono} > 1$) by the aggregation pro-
 595 cess and there is no source of monomers like nucleation considered (Figure 10a). This
 596 decrease of F_N (and increase of m_{mean}) is especially strong at heights between 2 km to
 597 3 km. This region of enhanced aggregation is found at heights where the temperature
 598 is close to $-15\text{ }^\circ\text{C}$ where the sticking efficiency has a local maximum. As a result of the
 599 conversion of monomers to aggregates, F_N of the aggregates increases at heights higher
 600 than about 3.5 km (Figure 10b). At lower heights the number of aggregate-aggregate
 601 collisions outweigh the number of monomer-monomer collisions and thus F_N of the ag-
 602 gregates decreases.

603 The signature of the conversion from monomers to aggregates is also seen in F_m
 604 of the monomers (Figure 10c). Especially in the region of enhanced aggregation, this leads
 605 to a strong decrease of F_m . In the heights above this region, depositional growth out-
 606 weighs the loss of mass of the monomers to the aggregates and thus, there is an increase
 607 of F_m with decreasing height. F_m of the aggregates increases monotonously due to both
 608 depositional growth of the aggregates and conversion from monomers to aggregates (Fig-
 609 ure 10d). In this setup, the change of F_m with height is governed by v_{term} and q_N at
 610 a given height. For example, a combination of low v_{term} and high q_N at upper layers leads

611 to a large increase in F_m . Simply speaking, a large number of slow falling ice crystals
 612 can grow efficiently by deposition which increases F_m .

613 **5.1 Sensitivity to Representation of Monomer Number Dependency**

614 The CTRL simulation is now compared to simulations with a binary separation
 615 into single-monomer particles and aggregates of any monomer number larger than 1 (bi-
 616 nary). An additional simulation is performed with no monomer number dependence (con-
 617 stant). Here the particle properties, that were fitted to the mean of all aggregates, are
 618 used for all particles. All simulations are done for plate and needle monomers and ag-
 619 gregates because we found the monomer dependence to be most pronounced for these
 620 monomer types. For the other monomer types the effect of N_{mono} can be expected to
 621 be smaller.

622 The most apparent difference between the simulations with different representa-
 623 tions of the N_{mono} dependencies for plate monomers and aggregates of plates is the faster
 624 decrease of F_N and F_m and faster increase of m_{mean} of the monomers ($N_{mono} = 1$) in
 625 the “constant” simulation (Figure 10). A slightly faster decrease of F_N (faster increase
 626 of m_{mean}) for aggregates ($N_{mono} > 1$) with decreasing height can be seen for both the
 627 “binary” and the “CTRL” simulation. However, all of the simulations show very sim-
 628 ilar profiles.

629 Figure 11 shows the same experiment as Figure 10 but using the parameterizations
 630 for needles instead of plates. Also for plates the most remarkable difference between the
 631 simulations is the difference between the “constant” and the “CTRL” run (Figure 11a
 632 and e). Also aggregate-aggregate collections are less effective in the “CTRL” run (Fig-
 633 ure 11b and f).

634 Overall, the differences of m_{mean} at the ground of the total ice particle population
 635 is small (factor of 1.2 and 1.4 higher m_{mean} for the “binary” and “constant” simulation
 636 for plates and factor of 0.8 lower m_{mean} for the “binary” and “constant” simulation for
 637 needles, Table 5).

638 Also the differences in the precipitation rates (F_m) are small (less than 5%; see Ta-
 639 ble 5). These small differences are due to the small difference of the absolute value of
 640 v_{term} at small sizes (Figure 7) and q_N at upper heights, which lead to a similar mass up-

641 take (Figure 10). However, the precipitation rate between the “Plate CTRL” simulation
 642 and the “Needle CTRL” simulation is relatively large (Table 5), which might be due to
 643 the strongly different v_{term} of the monomers.

644 The N_{mono} -dependency is even weaker for aggregates composed of other monomer
 645 types (Section 4.2 and 4.3). In summary, the simulation experiments with different monomer
 646 dependency indicate that a binary separation between single monomers and aggregates
 647 performs similarly well as relations which take into account a more detailed monomer
 648 dependency. Some but still small differences are found if no monomer dependency is taken
 649 into account, i.e. a single ice class for all monomer numbers is assumed. Hence we find
 650 that the classical separation in cloud ice (monomers) and snow (aggregates) is sufficient
 651 for the aspects of monomer number dependent particle properties.

652 5.2 Sensitivity to the Parameterization of Terminal Velocity

653 In this section, we test the sensitivity of the simulations to different implementa-
 654 tions of the $v_{term}-D_{max}$ formulation. In Figure 12, v_{term} of plate monomers and ag-
 655 gregates is parameterized either as power-law or Atlas-type fit.

656 As we saw in Figure 9, the power-law and Atlas-type fits match very closely at small
 657 particle sizes. This explains the very close matching of the three simulations in the up-
 658 per part of the simulated profiles (Figure 12) where the PSD is dominated by small par-
 659 ticles. As soon as the aggregation becomes stronger (below ca. 3 km), F_N in the sim-
 660 ulations using the power law (Figure 12b) is much lower than for Atlas-type. The de-
 661 creasing number flux of aggregates with lower height (Figure 12b) also indicates that es-
 662 pecially the self-collection of aggregates is stronger than for Atlas-type. In the same height
 663 region, the mean mass of the aggregates (Figure 12f) is strongly increased for the power
 664 law (factor of 5). As expected, the continuously increasing v_{term} in the power law leads
 665 to much stronger growth of aggregates as compared to relations which include the sat-
 666 uration velocity at large particle sizes. This is an interesting finding and could be one
 667 reason for the overestimation of radar reflectivities found at lower layers in ice clouds sim-
 668 ulated with the Seifert-Beheng scheme (Heinze et al., 2017).

669 Although m_{mean} of the aggregates is much larger for the power law, the difference
 670 to the Atlas-type in precipitation rates is very small (smaller than 5%; Figure 12d and
 671 Table 5). Note that in more realistic cases, as e.g. in presence of stronger sublimation

672 layers, the difference in m_{mean} can induce larger differences in the precipitation rate be-
 673 cause larger particles can fall through a thicker layer of subsaturated air before they sub-
 674 limate completely.

675 **6 Summary and Conclusions**

676 In this study, we generated a large ensemble of ice aggregates (ca. 105'000 parti-
 677 cles) using an aggregation model and hydrodynamic theory to study the change of par-
 678 ticle properties such as mass m , projected area A and terminal velocity v_{term} as a func-
 679 tion of monomer number N_{mono} and size. The aggregates were composed of various monomers
 680 types (plates, dendrites, needles and columns), monomer sizes and monomer numbers.
 681 In order to test the impact of habit mixtures, we also included in our analysis two dif-
 682 ferent mixtures of dendrites and columns. The choice of mixing specifically dendrites and
 683 columns was motivated by in-situ observations of the composing monomers in large ag-
 684 gregates sampled on the ground (Lawson et al., 1998).

685 When comparing our aggregate properties with in-situ observations, we find m and
 686 A to be very similar to the results presented in Mitchell et al. (1990) but the slope of
 687 our $m - D_{max}$ relations is larger than the slope given in Locatelli and Hobbs (1974).
 688 A better agreement with Locatelli and Hobbs (1974) and also with theoretical consid-
 689 erations in Westbrook et al. (2004b) are reached for mixtures of small columns and larger
 690 dendrites (Mix2). Interestingly, this monomer mixture also achieves the best agreement
 691 with observed $v_{term} - D_{max}$ relations. Considering the large spread in the observations
 692 (Figure 3), we can overall conclude that our aggregate ensemble matches the observed
 693 range of variability and does not show any substantial bias.

694 Our synthetic aggregate ensemble allowed us to investigate the transition of par-
 695 ticle properties from single crystals to aggregates with increasing number of monomers
 696 in a level of detail which is currently unavailable from in-situ observations. For m and
 697 A as a function of size we find the relations to change rather smoothly with increasing
 698 N_{mono} . The differences introduced by the choice of the monomer type are found to be
 699 overall larger than due to the number of monomers. We find the exponents in the $A-$
 700 D_{max} and $m - D_{max}$ relations of the monomers to be closely connected to the result-
 701 ing change with N_{mono} .

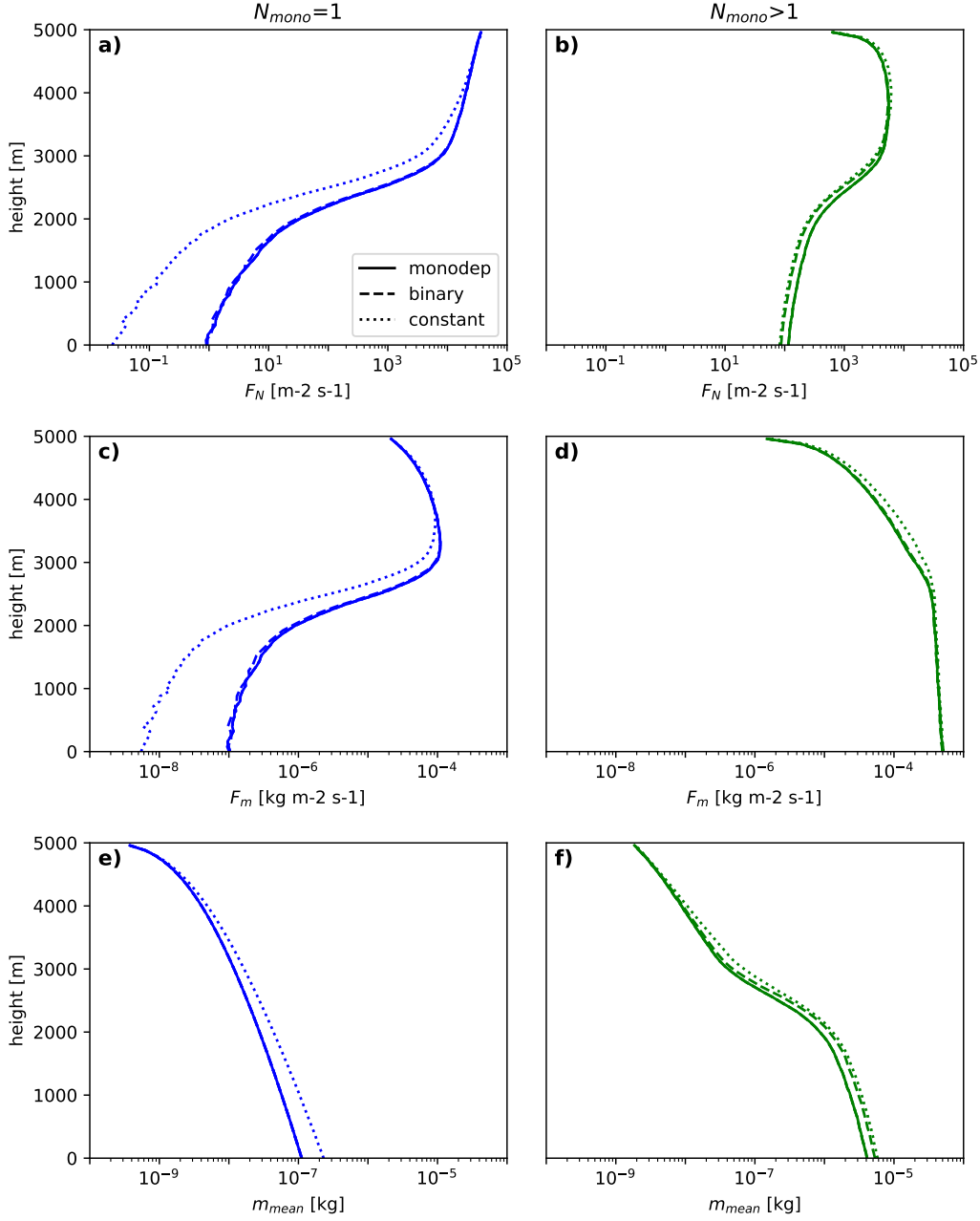


Figure 10. Idealized McSnow simulation using the N_{mono} dependent fit for plates (“monodep”; Table 3), the separation between $N_{mono} = 1$ and $N_{mono} > 1$ (“binary”; Tables 1 and 4) and single relation (the one fitted to all aggregates) for all N_{mono} (“constant”; Table 4) for plates. For each individual super-particle, B92 is used directly to calculate v_{term} . Shown are height profiles of (a, b) number flux F_N , (c, d) mass flux F_m and (e, f) mean mass m_{mean} . The particles are categorized into $N_{mono} = 1$ (left) and $N_{mono} > 1$ (right).

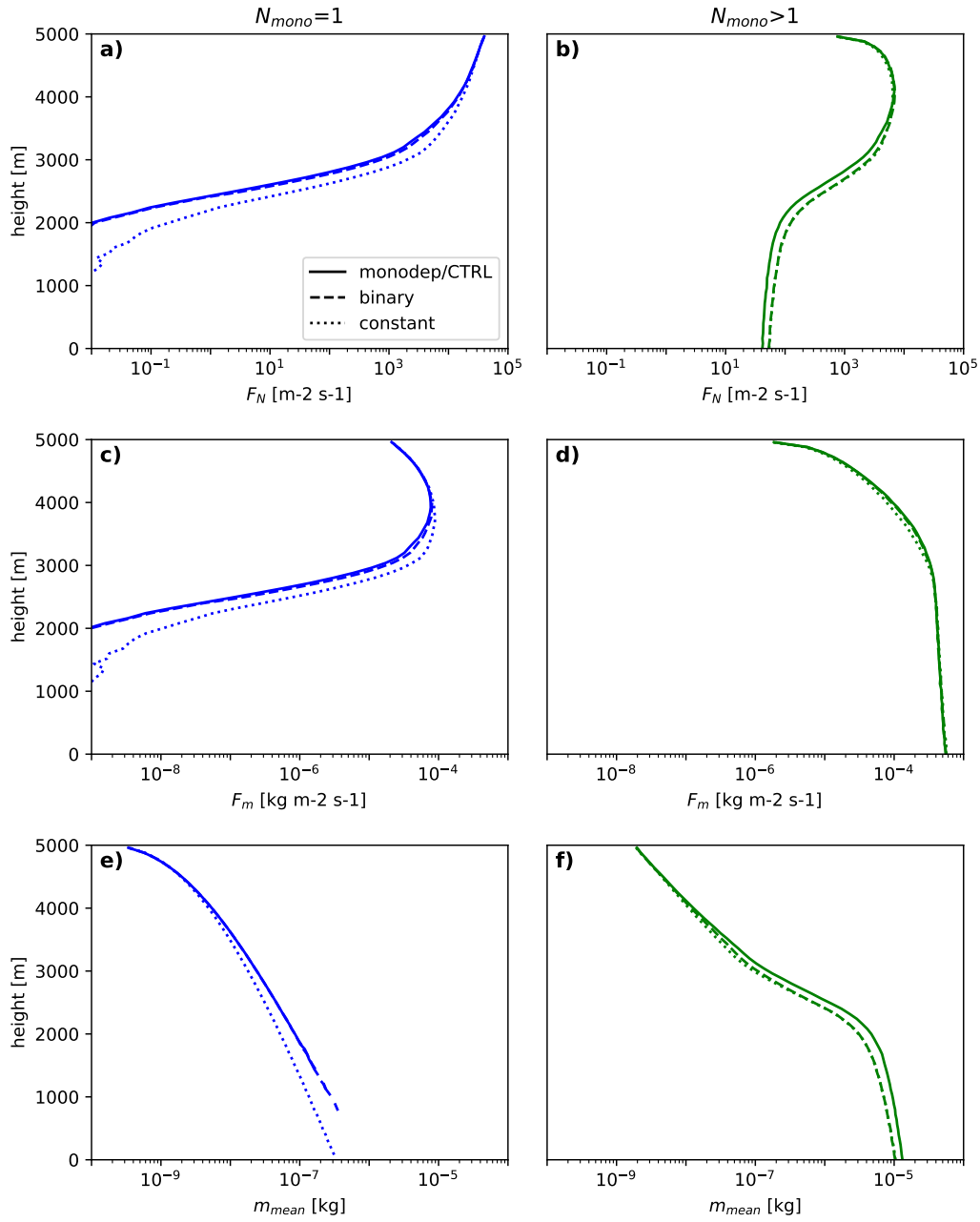


Figure 11. Same as Figure 10 but for needle monomers and aggregates.

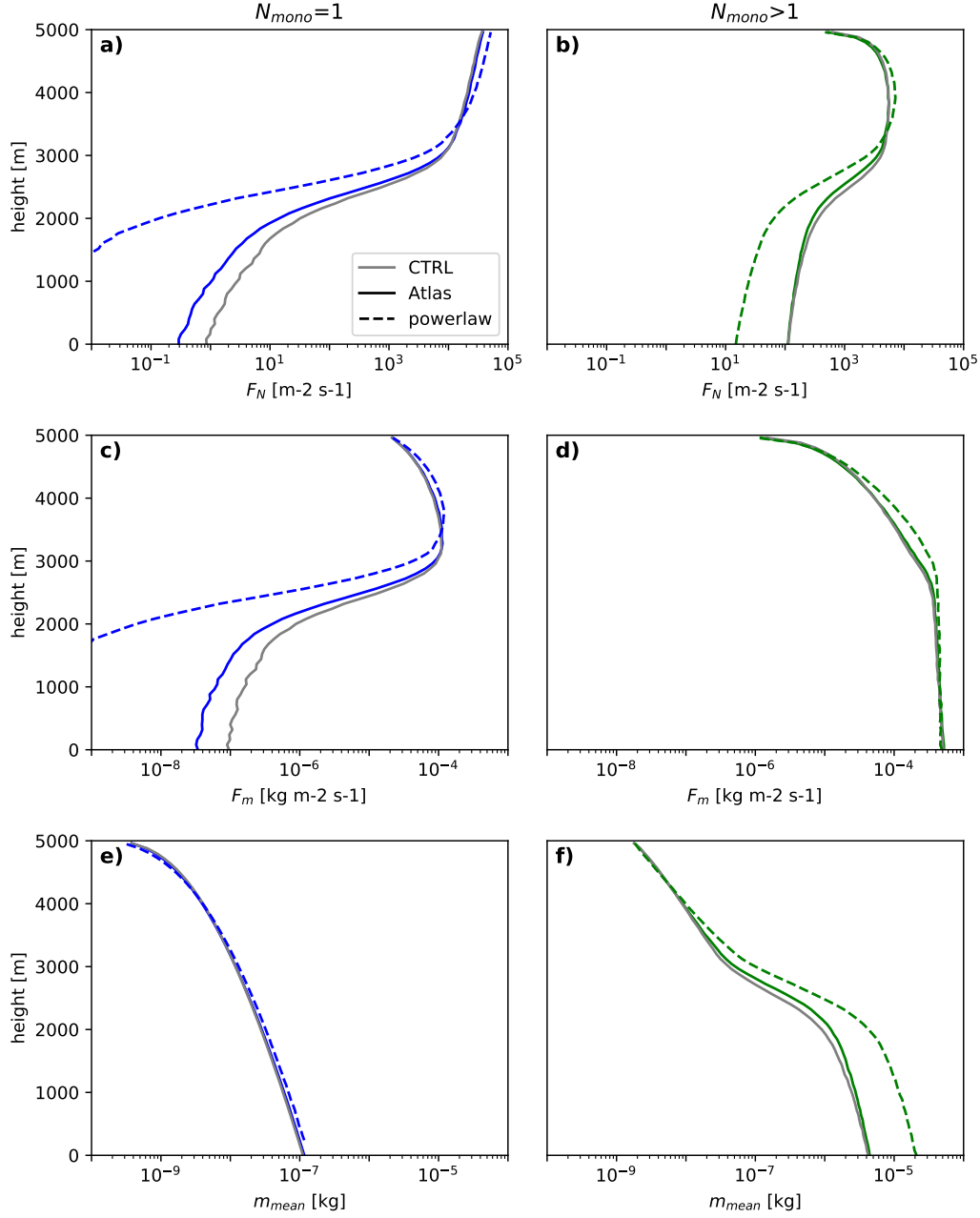


Figure 12. Idealized McSnow simulation using m - D_{max} and A - D_{max} for plate monomers and aggregates of plates (see Tables 1 and 4) and power law and Atlas-type v_{term} - D_{max} relations for plate monomers and aggregates of plates (see Table 5). Overlaid is the CTRL/monodep simulation in gray (see also Figure 10). Shown are height profiles of (a, b) number flux F_N (c,d), mass flux F_m (e,f) and mean mass m_{mean} . The particles are categorized into $N_{mono} = 1$ (left) and $N_{mono} > 1$ (right).

702 The derived $A-D_{max}$ and $m-D_{max}$ relations including the monomer type and
 703 number dependence were then used to calculate $v_{term}-D_{max}$ relations. Again, we find
 704 a rather smooth transition from single crystals to aggregates rather than a 'jump' as found
 705 in several microphysics schemes (Figure 1b). For small sizes below a few mm, our results
 706 suggests that the 'ice' and 'snow' category of microphysics schemes should have similar
 707 properties. At larger sizes, the aggregates v_{term} are found to deviate more from the monomers.
 708 Again, the monomer type is found to have a larger impact than the monomer number.
 709 Aggregates of plates tend to be faster while aggregates of needles are slower than the equal-
 710 size monomer. In accordance to in-situ observations, our simulations reveal for all ag-
 711 gregate types a saturation of v_{term} at cm sizes. However, the saturation value varies for
 712 the different aggregate types from 0.8 to 1.6 m s⁻¹.

713 In order to potentially implement our results in microphysics schemes, we derived
 714 two-parameter power-law fits and three-parameter Atlas-type fits for single monomers
 715 ($N_{mono} = 1$) and aggregates ($N_{mono} > 1$) representing the commonly used ice and
 716 snow classes in models. The new power-law fits match the small sizes well and avoid un-
 717 realistic 'jumps' found in current schemes. However, the power laws are unable to rep-
 718 resent the saturation of v_{term} at larger sizes. The Atlas-type fits are found to match the
 719 entire size range well and should thus be considered to be implemented in ice microphysics
 720 schemes as they do not substantially increase the computational costs while strongly im-
 721 proving the realism of the relations.

722 We finally tested the impact of implementing monomer dependence, habit type,
 723 and velocity fitting method on idealized aggregation simulations. For this, we used a new
 724 1D Lagrangian Monte Carlo model which allowed us to implement the derived relations
 725 with different degree of complexity. The simulations experiments revealed that there is
 726 only a very small impact of using a relation of only two monomer categories (single par-
 727 ticle and aggregate) as compared to a continuous monomer number dependence. A sin-
 728 gle category which does not take any monomer number into account shows slightly larger
 729 deviations but the variability due to monomer type is in general larger than the impact
 730 of monomer number.

731 In a second simulation experiment, we investigated the impact of using a power law
 732 or an Atlas-type fit for v_{term} . The simulations show very small differences in the upper
 733 part of the cloud where the profiles are dominated by small particles which are fitted sim-

734 ilarly well with the two relations. Once aggregation becomes more dominant and the spread
 735 of particles sizes shifts to larger sizes, the simulations using the power law lead to a much
 736 stronger aggregation and in particular stronger self-aggregation of particles as compared
 737 to the Atlas-type fit. The impact of the widely used power-law relations for v_{term} should
 738 thus be further studied for bulk schemes as it seems to be likely that they might cause
 739 an overestimation of aggregation and snow particle sizes.

740 We also shortly investigated the sensitivity of our derived relations to particle tum-
 741 bling and the choice of the hydrodynamic theory. While tumbling can significantly af-
 742 fect the properties of single monomers, it has a surprisingly small effect on our results
 743 for the aggregates. The choice of the hydrodynamic theory is a larger source of uncer-
 744 tainty which should be further investigated in future studies. It seems to be important
 745 in the future to better constraint the composition of aggregates regarding the monomer
 746 type. This question could be approached by improved in-situ techniques but also with
 747 detailed models that allow to predict the particle habit such as presented in e.g. Woods
 748 et al. (2007); Jensen et al. (2017); Shima et al. (2019).

749 **Appendix A Appendix**

750 **A1 Video-Disdrometer Dataset**

751 The terminal velocity v_{term} of the simulated aggregates from this study is compared
 752 to recent observations of falling ice particle properties and frequently used literature in
 753 Section 3.2. These surface observations are from the Centre for Atmospheric Research
 754 Experiments (CARE), Canada. It is a research facility of the Air Quality Research Branch
 755 of the Meteorological Service of Canada, located about 80 km north of Toronto, Ontario
 756 (lat = 44 13' 58" N, lon = 79 46 53" W). The instrumentation includes a video-disdrometer,
 757 Particle Imaging Package (PIP), precipitation weighing gauge, and meteorological mea-
 758 surements of e.g. wind velocity.

759 More detail about PIP can be found in von Lerber et al. (2017) and references therein.
 760 The particle sizes are recorded in the range of 0.2 - 26 mm (disk equivalent diameter)
 761 with a resolution of 0.2 mm, which is converted to the side projected D_{max} . In practice,
 762 the minimum reliable size with measurement of v_{term} is approximately 0.5 mm. Obser-
 763 vations of the side projected maximum dimension $D_{max,side}$ can be conducted from the
 764 gray-scale video images. The velocity v_{term} is obtained from the observations of the con-

765 secutive frames. The observed v_{term} utilized in the Figures 1a and 3c-d are separated
 766 from the whole dataset by limiting the exponent of the “5-minute m-D relation” between
 767 1.7-2.2 to exclude rimed particles (von Lerber et al., 2017). To apply this m-D thresh-
 768 old, the mass of the single particle and D_{max} has to be retrieved. The mass estimate of
 769 a single particle is calculated from the observed v_{term} , corrected D_{max} and area ratio
 770 using different parametrizations of the hydrodynamic theory (Böhm, 1989; Mitchell &
 771 Heymsfield, 2005; Heymsfield et al., 2010). For each snowfall event, each of these param-
 772 eterizations are calculated and the one which minimizes the error in the estimate of the
 773 liquid water equivalent precipitation with respect to the precipitation gauge is selected
 774 for that event. This procedure and the related uncertainties are described more in de-
 775 tail in von Lerber et al. (2017). Additionally observations during 5-minutes intervals, where
 776 the mean horizontal wind speed exceeds 4 m s^{-1} are excluded to reduce turbulence ef-
 777 fects (similar to Brandes et al. (2008)).

778 After applying these filters, the dataset, which covers the winters from 2014 to 2017
 779 with 48 snowfall events, contains about 4.3 million ice particles. It should be noted that
 780 PIP is providing a measurement of the ensemble of particles and no particle by particle-
 781 based classification is performed. Hence, the measurement volume includes mixtures of
 782 different habits.

783 **A2 Sensitivity of the Terminal Velocity to the Hydrodynamic Model** 784 **and Tumbling**

785 ***A21 Hydrodynamic Models***

786 As mentioned in Section 2.2, the hydrodynamic models of B92, KC05 and HW10
 787 differ in several aspects. The $Re(X)$ relation requires assumptions about particle sur-
 788 face roughness, which are differently implemented in the models. Also the definition of
 789 X is different (Table A1). While in B92 X is proportional to $mD_{max}^{0.5}A^{-0.25}$, X is pro-
 790 portional to $mD_{max}A^{-0.5}$ in HW10 and mD_{max}^2A in KC05. As a result in B92 and HW10,
 791 v_{term} increases slower with decreasing area ratio ($A_r = 4A\pi^{-1}D^{-2}$) than in the for-
 792 mulation of KC05. The empirical correction of X due to wake turbulence is also applied
 793 in KC05 but not in HW10.

794 These differences affect the behaviour of v_{term} at large sizes and the monomer num-
 795 ber dependency (which we quantify by $s_{monodep}$). Without the empirical correction of

	B92	HW10	KC05
$X \sim$	$mD_{max}^{0.5}A^{-0.25}$	$mD_{max}A^{-0.5}$	mD_{max}^2A
$v_{term, Re \ll 1} \sim$	$D_{max}^{b_m - 0.25b_A - 0.5}$	$D_{max}^{b_m - 0.5b_A}$	$D_{max}^{b_m - b_A + 1}$
$v_{term, Re \gg 1} \sim$	$(D_{max}^{b_m - 0.25b_A - 1.5})^{0.5}$	$(D_{max}^{b_m - 0.5d - 1})^{0.5}$	$(D_{max}^{b_m - b_A})^{0.5}$
$s_{monodep} =$	$b_{m,agg} - b_{m,1}$ $-0.25(b_{A,agg} - d_{m,1})$	$b_{m,agg} - b_{m,1}$ $-0.5(b_{A,agg} - b_{A,1})$	$b_{m,agg} - b_{m,1}$ $-(b_{A,agg} - b_{A,1})$

Table A1. Proportionality of the Best number X on the particle properties (mass m and projected area A), scaling relations of the $v_{term} - D_{max}$ relations and $s_{monodep}$ in different hydrodynamic models (Böhm (1992) B92, Heymsfield et al. (2010) HW10, Khvorostyanov and Curry (2005) KC05). The derivation of the scaling relations is shown exemplary for B92 in Section 2.2. $s_{monodep}$, which gives an estimate of the sign and strength of the dependency of v_{term} on N_{mono} is defined in Section 4.3.

796 X (which considers wake turbulence), v_{term} only saturates if $v_{term, Re \gg 1} \sim D^0$. For
 797 example with HW10 the saturation would be reached for $b_m - 0.5b_A - 1 = 0$ (Table
 798 A1). This is e.g. not the case for aggregates of plates simulated in this study and there-
 799 fore HW10 does not predict a saturation of v_{term} at larger sizes (Figure A1a).

800 Also the sign and the strength of the increase/decrease of v_{term} with increasing N_{mono}
 801 depends on the formulation of X . In Section 4.3 we introduced $s_{monodep}$ as a measure
 802 for this monomer number dependency. Applying this measure to the aggregates of plates
 803 yields $s_{monodep} = -0.21$ for HW10 and $s_{monodep} = -0.06$ for KC05. Both HW10 and
 804 KC05 show the decrease of v_{term} with increasing N_{mono} which we saw when using B92,
 805 but this decrease is very weak for KC05.

806 **A22 Tumbling**

807 To investigate the effect of the tumbling of the aggregates (as reported e.g. by Garrett
 808 and Yuter (2014a)) on the projected area A and v_{term} , the particles are tilted with a stan-
 809 dard deviation of 0° , 20° , 40° and 60° , around the principal axis (Figure A2). This is
 810 done only after the final aggregate is assembled and thereby does not influence the struc-
 811 ture of the aggregates. This rotation reduces A and in turn, v_{term} increases.

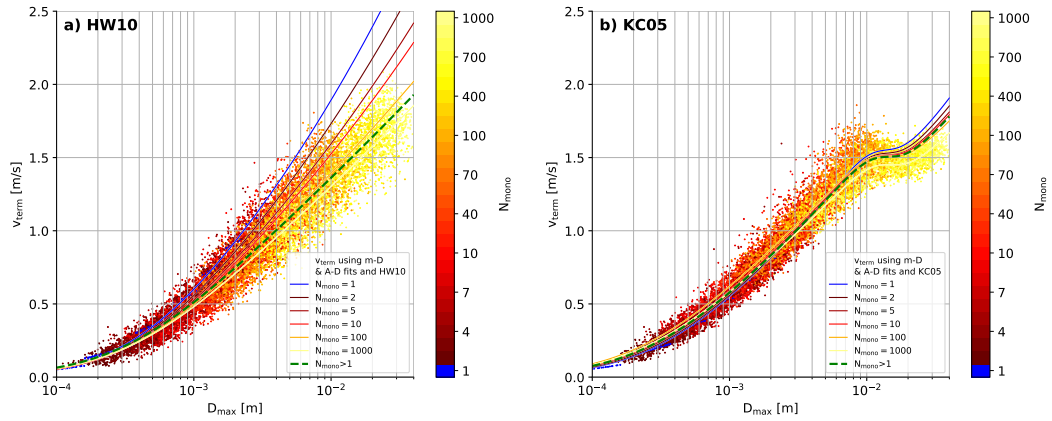


Figure A1. Same as Figure 7a (aggregates of plates) but using HW10 in a) and KC05 in b)

812 The monomers (top panel in Figure A2) are stronger effected by tumbling (espe-
 813 cially at large D_{max}) due to their lower aspect ratio (not shown). The largest increase
 814 in v_{term} with increasing tumbling is found for KC05 due to the largest increase in the
 815 Best number with decreasing A (see Section 2.2). B92 shows the least influence of tum-
 816 bling, which increases v_{term} at maximum by about 0.1 m s^{-1} and has a negligible effect
 817 on v_{term} for the aggregates.

818 Acknowledgments

819 Contributions by M.K., S.K. and D.O. were funded by the German Research Founda-
 820 tion (DFG) under grant KN 1112/2-1 as part of the Emmy-Noether Group Optimal com-
 821 bination of Polarimetric and Triple Frequency radar techniques for Improving Microphys-
 822 ical process understanding of cold clouds (OPTIMIce). A.v.L. gratefully acknowledges
 823 the funding by the Deutsche Forschungsgemeinschaft (DFG, German Research Founda-
 824 tion) Project-ID 268020496 TRR 172, within the Transregional Collaborative Research
 825 Center ‘‘ArctiC Amplification: Climate Relevant Atmospheric and SurfaCe Processes,
 826 and Feedback Mechanisms (AC)³’’. M.K. also acknowledges support by the Graduate
 827 School of Geosciences of the University of Cologne. The source code of McSnow used in
 828 this study is hosted at GitLab, and access can be granted by A. S. on request. We also
 829 thank Jussi Leinonen for fruitful discussions and for making his aggregation model freely
 830 available at GitHub (<https://github.com/jleinonen/aggregation>). We thank David
 831 Hudak and Peter Rodriguez from Environment Canada for providing the PIP measure-

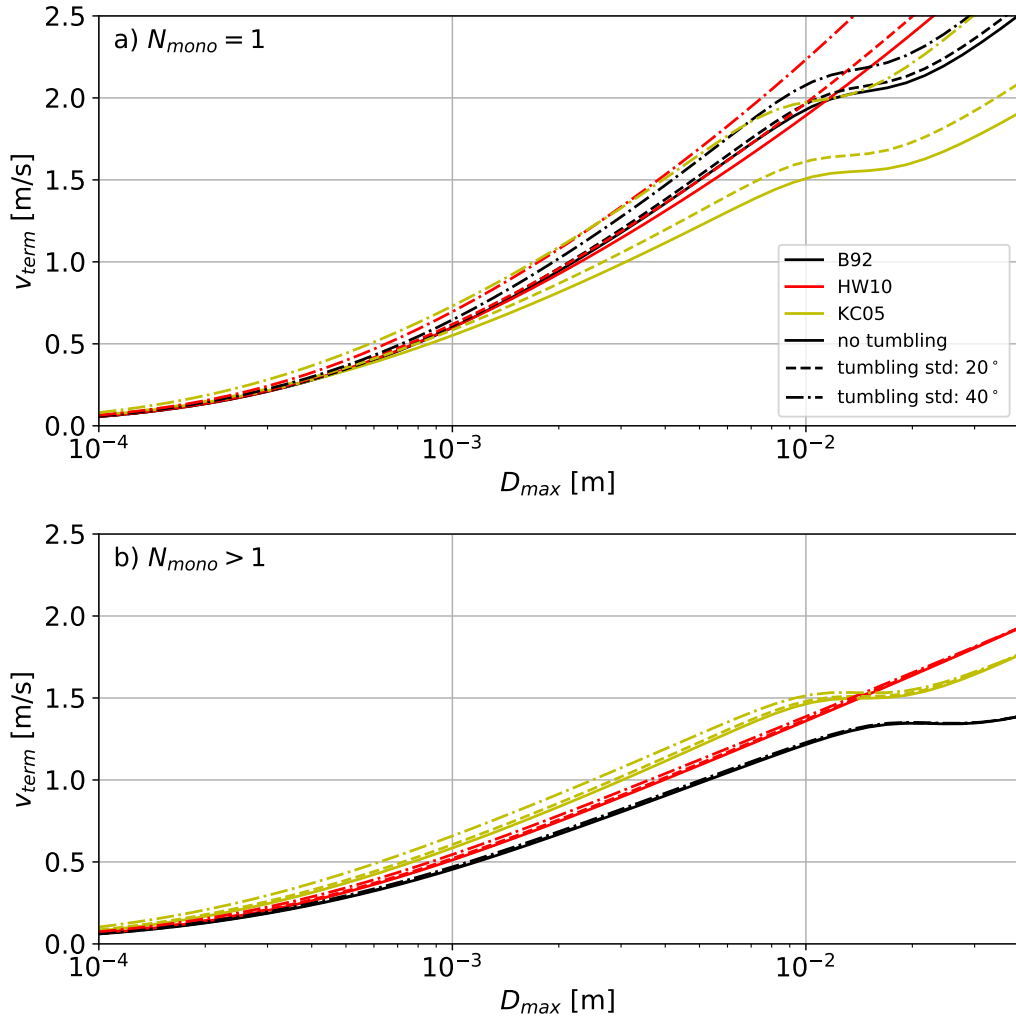


Figure A2. v_{term} based on m/A-D fits (Table 1 and Table 4) and different hydrodynamic models. The particles are horizontally aligned (“no tumbling”) rotated by 20° or 40° around the principal axis to mimic different strength of tumbling. a) plate monomers; b) aggregates of plates

832 ment from the CARE site. The CARE site is part of the NASA GPM (Global Precip-
 833 itation Measurement) Ground Validation (GV) program. Model output data of the ag-
 834 gregation model and McSnow are accessible at the ZENODO platform ([https://doi](https://doi.org/10.5281/zenodo.3606668)
 835 [.org/10.5281/zenodo.3606668](https://doi.org/10.5281/zenodo.3606668)).

836 References

- 837 Abraham, F. F. (1970). Functional dependence of drag coefficient of a sphere
 838 on reynolds number. *Physics of Fluids*, *13*(8), 2194–2195. doi: 10.1063/
 839 1.1693218
- 840 Atlas, D., Srivastava, R. C., & Sekhon, R. S. (1973, feb). Doppler radar charac-
 841 teristics of precipitation at vertical incidence. *Reviews of Geophysics*, *11*(1), 1.
 842 Retrieved from <http://doi.wiley.com/10.1029/RG011i001p00001> doi: 10
 843 .1029/RG011i001p00001
- 844 Bailey, M. P., & Hallett, J. (2009). A Comprehensive Habit Diagram for At-
 845 mospheric Ice Crystals: Confirmation from the Laboratory, AIRS II, and
 846 Other Field Studies. *Journal of the Atmospheric Sciences*, *66*(9), 2888–
 847 2899. Retrieved from [http://journals.ametsoc.org/doi/abs/10.1175/](http://journals.ametsoc.org/doi/abs/10.1175/2009JAS2883.1)
 848 [2009JAS2883.1](http://journals.ametsoc.org/doi/abs/10.1175/2009JAS2883.1) doi: 10.1175/2009JAS2883.1
- 849 Barthazy, E., Göke, S., Schefold, R., & Högl, D. (2004). An optical array in-
 850 strument for shape and fall velocity measurements of hydrometeors. *Jour-*
 851 *nal of Atmospheric and Oceanic Technology*, *21*(9), 1400–1416. doi:
 852 10.1175/1520-0426(2004)021<1400:AOAIFS>2.0.CO;2
- 853 Barthazy, E., & Schefold, R. (2006). Fall velocity of snowflakes of different riming
 854 degree and crystal types. *Atmospheric Research*, *82*(1-2), 391–398. doi: 10
 855 .1016/j.atmosres.2005.12.009
- 856 Bernauer, F., Hürkamp, K., Rühm, W., & Tschiersch, J. (2016, may). Snow event
 857 classification with a 2D video disdrometer - A decision tree approach. *Atmo-*
 858 *spheric Research*, *172-173*, 186–195. doi: 10.1016/j.atmosres.2016.01.001
- 859 Böhm, J. (1989). *A general equation for the terminal fall speed of solid hydrometeors*
 860 (Vol. 46) (No. 15). Retrieved from [http://journals.ametsoc.org/doi/abs/](http://journals.ametsoc.org/doi/abs/10.1175/1520-0469(1989)046(2419:AGEFTT)2.0.CO;2)
 861 [10.1175/1520-0469\(1989\)046\(2419:AGEFTT\)2.0.CO;2](http://journals.ametsoc.org/doi/abs/10.1175/1520-0469(1989)046(2419:AGEFTT)2.0.CO;2)
 862 [.0.CO;2](http://journals.ametsoc.org/doi/abs/10.1175/1520-0469(1989)046(2419:AGEFTT)2.0.CO;2) doi: 10.1175/1520-0469(1989)046(2419:AGEFTT)2.0.CO;2
- 863 Böhm, J. (1992). A general hydrodynamic theory for mixed-phase microphysics.

- 864 Part I: Drag and fall speed of hydrometeors. *Atmospheric research*, 27(4),
 865 253–274.
- 866 Brandes, E. A., Ikeda, K., Thompson, G., & Schönhuber, M. (2008, oct). Aggregate
 867 terminal velocity/temperature relations. *Journal of Applied Meteorology and*
 868 *Climatology*, 47(10), 2729–2736. Retrieved from [http://journals.ametsoc](http://journals.ametsoc.org/doi/abs/10.1175/2008JAMC1869.1)
 869 [.org/doi/abs/10.1175/2008JAMC1869.1](http://journals.ametsoc.org/doi/abs/10.1175/2008JAMC1869.1) doi: 10.1175/2008JAMC1869.1
- 870 Brdar, S., & Seifert, A. (2018). McSnow: A Monte-Carlo Particle Model for Riming
 871 and Aggregation of Ice Particles in a Multidimensional Microphysical Phase
 872 Space. *Journal of Advances in Modeling Earth Systems*, 10(1), 187–206. doi:
 873 10.1002/2017MS001167
- 874 Brown, S. R. (1970). *TERMINAL VELOCITIES OF ICE CRYSTALS* (Tech.
 875 Rep.). Fort Collins, Colorado: Department of Atmospheric Science Colorado
 876 State University.
- 877 Bürgesser, R. E., Giovacchini, J. P., & Castellano, N. E. (2019, oct). Sedimen-
 878 tation analysis of columnar ice crystals in viscous flow regimes. *Quar-*
 879 *terly Journal of the Royal Meteorological Society*, qj.3684. Retrieved from
 880 <https://onlinelibrary.wiley.com/doi/abs/10.1002/qj.3684> doi:
 881 10.1002/qj.3684
- 882 Connolly, P. J., Emersic, C., & Field, P. R. (2012). A laboratory investigation into
 883 the aggregation efficiency of small ice crystals. *Atmospheric Chemistry and*
 884 *Physics*, 12(4), 2055–2076. doi: 10.5194/acp-12-2055-2012
- 885 Cornford, S. G. (1965, jan). Fall speeds of precipitation elements. *Quarterly Journal*
 886 *of the Royal Meteorological Society*, 91(387), 91–94. Retrieved from [http://](http://doi.wiley.com/10.1002/qj.49709138713)
 887 doi.wiley.com/10.1002/qj.49709138713 doi: 10.1002/qj.49709138713
- 888 Frick, C., Seifert, A., & Wernli, H. (2013). A bulk parametrization of melting
 889 snowflakes with explicit liquid water fraction for the COSMO model. *Geosci-*
 890 *entific Model Development*, 6(6), 1925–1939. doi: 10.5194/gmd-6-1925-2013
- 891 Garrett, T. J., Fallgatter, C., Shkurko, K., & Howlett, D. (2012, nov). Fall speed
 892 measurement and high-resolution multi-angle photography of hydromete-
 893 ors in free fall. *Atmospheric Measurement Techniques*, 5(11), 2625–2633.
 894 Retrieved from <https://www.atmos-meas-tech.net/5/2625/2012/> doi:
 895 10.5194/amt-5-2625-2012
- 896 Garrett, T. J., & Yuter, S. E. (2014a). Observed influence of riming, temperature,

- 897 and turbulence on the fallspeed of solid precipitation. *Geophysical Research*
898 *Letters*, 41(18), 6515–6522. doi: 10.1002/2014GL061016
- 899 Garrett, T. J., & Yuter, S. E. (2014b, sep). Observed influence of riming, temper-
900 ature, and turbulence on the fallspeed of solid precipitation. *Geophysical Re-*
901 *search Letters*, 41(18), 6515–6522. Retrieved from [http://doi.wiley.com/10](http://doi.wiley.com/10.1002/2014GL061016)
902 [.1002/2014GL061016](http://doi.wiley.com/10.1002/2014GL061016) doi: 10.1002/2014GL061016
- 903 Hashino, T., Cheng, K. Y., Chueh, C. C., & Wang, P. K. (2016, may). Nu-
904 merical study of motion and stability of falling columnar crystals. *Jour-*
905 *nal of the Atmospheric Sciences*, 73(5), 1923–1942. Retrieved from
906 <http://journals.ametsoc.org/doi/10.1175/JAS-D-15-0219.1> doi:
907 [10.1175/JAS-D-15-0219.1](http://journals.ametsoc.org/doi/10.1175/JAS-D-15-0219.1)
- 908 Hashino, T., & Tripoli, G. J. (2011). The Spectral Ice Habit Prediction System
909 (SHIPS). Part IV: Box model simulations of the habit-dependent aggregation
910 process. *Journal of the Atmospheric Sciences*, 68(6), 1142–1161. Retrieved
911 from <http://journals.ametsoc.org/doi/abs/10.1175/2011JAS3667.1> doi:
912 [10.1175/2011JAS3667.1](http://journals.ametsoc.org/doi/abs/10.1175/2011JAS3667.1)
- 913 Heinze, R., Dipankar, A., Henken, C. C., Moseley, C., Sourdeval, O., Trömel, S., ...
914 Quaas, J. (2017). Large-eddy simulations over Germany using ICON: a com-
915 prehensive evaluation. *Quarterly Journal of the Royal Meteorological Society*,
916 143(702), 69–100. doi: 10.1002/qj.2947
- 917 Heymsfield, A. J. (1972, oct). Ice Crystal Terminal Velocities. *Journal of the At-*
918 *mospheric Sciences*, 29(7), 1348–1357. doi: 10.1175/1520-0469(1972)029<1348:
919 ictv>2.0.co;2
- 920 Heymsfield, A. J., Schmitt, C., Bansemer, A., & Twohy, C. H. (2010, oct). Im-
921 proved representation of ice particle masses based on observations in natural
922 clouds. *Journal of the Atmospheric Sciences*, 67(10), 3303–3318. Retrieved
923 from <http://journals.ametsoc.org/doi/abs/10.1175/2010JAS3507.1> doi:
924 [10.1175/2010JAS3507.1](http://journals.ametsoc.org/doi/abs/10.1175/2010JAS3507.1)
- 925 Jakob, C. (2002). Ice clouds in numerical weather prediction models - Progress,
926 problems and prospects. *Cambridge ; New York : Oxford University Press*,
927 327–345. Retrieved from [https://books.google.de/books?hl=de{\&}lr={\&}id=58v1fg4xeo8C{\&}oi=fnd{\&}pg=PA327{\&}dq=Ice+clouds+in+](https://books.google.de/books?hl=de&lr={\&}id=58v1fg4xeo8C{\&}oi=fnd{\&}pg=PA327{\&}dq=Ice+clouds+in+numerical+weather+prediction+models:+progress,+problems,+and+)
928 [numerical+weather+prediction+models:+progress,+problems,+and+](https://books.google.de/books?hl=de&lr={\&}id=58v1fg4xeo8C{\&}oi=fnd{\&}pg=PA327{\&}dq=Ice+clouds+in+numerical+weather+prediction+models:+progress,+problems,+and+)
929

- 930 prospects&ots={\ }1sSkM3vRL&sig=1vBgpnvEOsyd0CRJHHH-FeH5cHc
- 931 Jensen, A. A., Harrington, J. Y., Morrison, H., & Milbrandt, J. A. (2017,
 932 jun). Predicting ice shape evolution in a bulk microphysics model. *Jour-*
 933 *nal of the Atmospheric Sciences*, 74(6), 2081–2104. Retrieved from
 934 <http://journals.ametsoc.org/doi/10.1175/JAS-D-16-0350.1> doi:
 935 10.1175/JAS-D-16-0350.1
- 936 Kajikawa, M. (1972). Measurement of Falling Velocity of Individual Snow Crys-
 937 tals. *Journal of the Meteorological Society of Japan. Ser. II*, 50(6), 577–584.
 938 Retrieved from [https://www.jstage.jst.go.jp/article/jmsj1965/50/6/
 939 50{ }6{ }577/{ }article](https://www.jstage.jst.go.jp/article/jmsj1965/50/6/50{ }6{ }577/{ }article) doi: 10.2151/jmsj1965.50.6.577
- 940 Khain, A. P., Beheng, K. D., Heymsfield, A. J., Korolev, A., Krichak, S. O., Levin,
 941 Z., ... Yano, J. I. (2015). Representation of microphysical processes in cloud-
 942 resolving models: Spectral (bin) microphysics versus bulk parameterization.
 943 *Reviews of Geophysics*, 53(2), 247–322. doi: 10.1002/2014RG000468
- 944 Khvorostyanov, V. I., & Curry, J. A. (2005). Fall velocities of hydrometeors in the
 945 atmosphere: Refinements to a continuous analytical power law. *Journal of the
 946 Atmospheric Sciences*, 62(12), 4343–4357. doi: 10.1175/JAS3622.1
- 947 Kruger, A., & Krajewski, W. F. (2002, may). Two-dimensional video disdrometer:
 948 A description. *Journal of Atmospheric and Oceanic Technology*, 19(5), 602–
 949 617. Retrieved from [http://journals.ametsoc.org/doi/abs/10.1175/1520
 950 -0426{ }282002{ }29019{ }3C0602{ }3ATDVDAD{ }3E2.0.CO{ }3B2](http://journals.ametsoc.org/doi/abs/10.1175/1520-0426{ }282002{ }29019{ }3C0602{ }3ATDVDAD{ }3E2.0.CO{ }3B2)
 951 doi: 10.1175/1520-0426(2002)019<0602:TDVDAD>2.0.CO;2
- 952 Langleben, M. P. (1954). The terminal velocity of snowflakes. *Quarterly Jour-*
 953 *nal of the Royal Meteorological Society*, 80(344), 174–181. doi: 10.1002/
 954 qj.49708034404
- 955 Lawson, R. P., Stewart, R. E., & Angus, L. J. (1998). Observations and numeri-
 956 cal simulations of the origin and development of very large snowflakes. *Journal
 957 of the Atmospheric Sciences*, 55(21), 3209–3229. doi: 10.1175/1520-0469(1998)
 958 055(3209:OANSOT)2.0.CO;2
- 959 Leinonen, J. (2013). *Impact of the microstructure of precipitation and hydrometeors
 960 on multi-frequency radar observations* (No. May). Aalto University.
- 961 Leinonen, J., Kneifel, S., & Hogan, R. J. (2018). Evaluation of the RayleighGans ap-
 962 proximation for microwave scattering by rimed snowflakes. *Quarterly Journal*

- 963 of the *Royal Meteorological Society*, 144, 77–88. doi: 10.1002/qj.3093
- 964 Leinonen, J., & Moisseev, D. (2015). What do triple-frequency radar signatures
965 reveal about aggregate snowflakes? *Journal of Geophysical Research*, 120(1),
966 229–239. doi: 10.1002/2014JD022072
- 967 Leinonen, J., Moisseev, D., Leskinen, M., & Petersen, W. A. (2012, feb). A clima-
968 tology of disdrometer measurements of rainfall in finland over five years with
969 implications for global radar observations. *Journal of Applied Meteorology and*
970 *Climatology*, 51(2), 392–404. Retrieved from [http://journals.ametsoc.org/](http://journals.ametsoc.org/doi/abs/10.1175/JAMC-D-11-056.1)
971 doi/abs/10.1175/JAMC-D-11-056.1 doi: 10.1175/JAMC-D-11-056.1
- 972 Leinonen, J., & Szyrmer, W. (2015, aug). Radar signatures of snowflake rim-
973 ing: A modeling study. *Earth and Space Science*, 2(8), 346–358. Re-
974 trieved from <http://doi.wiley.com/10.1002/2015EA000102> doi:
975 10.1002/2015EA000102
- 976 Locatelli, J. D., & Hobbs, P. V. (1974). Fall speeds and masses of solid pre-
977 cipitation particles. *Journal of Geophysical Research*, 79(15), 2185–2197.
978 Retrieved from <http://doi.wiley.com/10.1029/JC079i015p02185> doi:
979 10.1029/jc079i015p02185
- 980 Mitchell, D. L., & Heymsfield, A. J. (2005). Refinements in the treatment of ice par-
981 ticle terminal velocities, highlighting aggregates. *Journal of the Atmospheric*
982 *Sciences*, 62(5), 1637–1644. Retrieved from [http://adsabs.harvard.edu/](http://adsabs.harvard.edu/abs/2005JAAtS...62.1637M)
983 abs/2005JAAtS...62.1637M{\%}0Ahttp://journals.ametsoc.org/doi/pdf/
984 10.1175/JAS3413.1 doi: 10.1175/JAS3413.1
- 985 Mitchell, D. L., Zhang, R., & Pitter, R. L. (1990). Mass-dimensional relationships
986 for ice particles and the influence of riming on snowfall rates. *Journal of Ap-*
987 *plied Meteorology*, 29(2), 153–163. doi: 10.1175/1520-0450(1990)029<0153:
988 MDRFIP>2.0.CO;2
- 989 Morales, A., Posselt, D. J., Morrison, H., & He, F. (2019). Assessing the influence
990 of microphysical and environmental parameter perturbations on orographic
991 precipitation. *Journal of the Atmospheric Sciences*, 76(5), 1373–1395. doi:
992 10.1175/JAS-D-18-0301.1
- 993 Morrison, H., Curry, J. A., & Khvorostyanov, V. I. (2005). A new double-moment
994 microphysics parameterization for application in cloud and climate models.
995 Part I: Description. *Journal of the Atmospheric Sciences*, 62(6), 1665–1677.

- 996 Retrieved from <http://journals.ametsoc.org/doi/abs/10.1175/JAS3446.1>
997 doi: 10.1175/JAS3446.1
- 998 Morrison, H., & Milbrandt, J. A. (2015, jan). Parameterization of cloud micro-
999 physics based on the prediction of bulk ice particle properties. Part I: Scheme
1000 description and idealized tests. *Journal of the Atmospheric Sciences*, *72*(1),
1001 287–311. Retrieved from [http://journals.ametsoc.org/doi/10.1175/
1002 JAS-D-14-0065.1](http://journals.ametsoc.org/doi/10.1175/JAS-D-14-0065.1) doi: 10.1175/JAS-D-14-0065.1
- 1003 Nakaya, U., & Terada, T. J. (1935, jan). Simultaneous Observations of the Mass,
1004 Falling Velocity and Form of Individual Snow Crystals. , *1*(7), 191–200.
- 1005 Nettesheim, J. J., & Wang, P. K. (2018). A numerical study on the aerodynamics of
1006 freely falling planar Ice Crystals. *Journal of the Atmospheric Sciences*, *75*(9),
1007 2849–2865. doi: 10.1175/JAS-D-18-0041.1
- 1008 Newman, A. J., Kucera, P. A., & Bliven, L. F. (2009, feb). Presenting the Snowflake
1009 Video Imager (SVI). *Journal of Atmospheric and Oceanic Technology*, *26*(2),
1010 167–179. Retrieved from [http://journals.ametsoc.org/doi/abs/10.1175/
1011 2008JTECHA1148.1](http://journals.ametsoc.org/doi/abs/10.1175/2008JTECHA1148.1) doi: 10.1175/2008JTECHA1148.1
- 1012 Ori, D., Maestri, T., Rizzi, R., Cimini, D., Montopoli, M., & Marzano, F. S. (2014,
1013 aug). Scattering properties of modeled complex snowflakes and mixed-phase
1014 particles at microwave and millimeter frequencies. *Journal of Geophysical Re-
1015 search: Atmospheres*, *119*(16), 9931–9947. Retrieved from [http://doi.wiley
1016 .com/10.1002/2014JD021616](http://doi.wiley.com/10.1002/2014JD021616) doi: 10.1002/2014JD021616
- 1017 Pruppacher, H. R., & Klett, J. D. (2010). *Microphysics of Clouds and Precipitation*.
1018 Springer Science + Business Media B.V.
- 1019 Przybylo, V. M., Sulia, K. J., Schmitt, C. G., Lebo, Z. J., & May, W. C. (2019).
1020 The ice Particle and Aggregate Simulator (IPAS). Part I: Extracting di-
1021 mensional properties of ice-ice aggregates for microphysical parameteriza-
1022 tion. *Journal of the Atmospheric Sciences*, *76*(6), 1661–1676. Retrieved
1023 from <http://journals.ametsoc.org/doi/10.1175/JAS-D-18-0187.1> doi:
1024 10.1175/JAS-D-18-0187.1
- 1025 Sanderson, B. M., Piani, C., Ingram, W. J., Stone, D. A., & Allen, M. R. (2008,
1026 feb). Towards constraining climate sensitivity by linear analysis of feedback
1027 patterns in thousands of perturbed-physics GCM simulations. *Climate Dynam-
1028 ics*, *30*(2-3), 175–190. Retrieved from <http://link.springer.com/10.1007/>

- 1029 s00382-007-0280-7 doi: 10.1007/s00382-007-0280-7
- 1030 Schmidt, G. A., Bader, D., Donner, L. J., Elsaesser, G. S., Golaz, J. C., Hannay, C.,
1031 ... Saha, S. (2017, sep). Practice and philosophy of climate model tuning
1032 across six US modeling centers. *Geoscientific Model Development*, 10(9), 3207–
1033 3223. Retrieved from <https://www.geosci-model-dev.net/10/3207/2017/>
1034 doi: 10.5194/gmd-10-3207-2017
- 1035 Schmitt, C. G., Sulia, K. J., Lebo, Z. J., Heymsfield, A. J., Przybyo, V., & Con-
1036 nolly, P. (2019, aug). The Fall Speed Variability of Similarly Sized Ice Par-
1037 ticle Aggregates. *Journal of Applied Meteorology and Climatology*, 58(8),
1038 1751–1761. Retrieved from [http://journals.ametsoc.org/doi/10.1175/](http://journals.ametsoc.org/doi/10.1175/JAMC-D-18-0291.1)
1039 JAMC-D-18-0291.1 doi: 10.1175/JAMC-D-18-0291.1
- 1040 Seifert, A., & Beheng, K. D. (2006). A two-moment cloud microphysics parameteri-
1041 zation for mixed-phase clouds. Part 1: Model description. *Meteorology and At-*
1042 *mospheric Physics*, 92(1-2), 45–66. doi: 10.1007/s00703-005-0112-4
- 1043 Seifert, A., Blahak, U., & Buhr, R. (2014). On the analytic approximation of bulk
1044 collision rates of non-spherical hydrometeors. *Geoscientific Model Develop-*
1045 *ment*, 7(2), 463–478. doi: 10.5194/gmd-7-463-2014
- 1046 Seifert, A., Leinonen, J., Siewert, C., & Kneifel, S. (2019, mar). The Geometry of
1047 Rimed Aggregate Snowflakes: A Modeling Study. *Journal of Advances in Mod-*
1048 *eling Earth Systems*, 11(3), 712–731. doi: 10.1029/2018MS001519
- 1049 Shima, S.-i., Kusano, K., Kawano, A., Sugiyama, T., & Kawahara, S. (2009). The
1050 super-droplet method for the numerical simulation of clouds and precipita-
1051 tion: A particle-based and probabilistic microphysics model coupled with a
1052 non-hydrostatic model. *Quarterly Journal of the Royal Meteorological Society*,
1053 135(642), 1307–1320. doi: 10.1002/qj.441
- 1054 Shima, S.-i., Sato, Y., Hashimoto, A., & Ryohei Misumi. (2019). GMDD -
1055 Predicting the morphology of ice particles in deep convection using the
1056 super-droplet method: development and evaluation of SCALE-SDM 0.2.5-
1057 2.2.0/2.2.1. *Geosci. Model Dev. Discuss.* Retrieved from [https://](https://www.geosci-model-dev-discuss.net/gmd-2019-294/{\#}discussion)
1058 www.geosci-model-dev-discuss.net/gmd-2019-294/{\#}discussion
- 1059 Szyrmer, W., & Zawadzki, I. (2010, oct). Snow studies. Part II: Average relation-
1060 ship between mass of snowflakes and their terminal fall velocity. *Journal of the*
1061 *Atmospheric Sciences*, 67(10), 3319–3335. Retrieved from <http://journals>

1062 .ametsoc.org/doi/abs/10.1175/2010JAS3390.1 doi: 10.1175/2010JAS3390
1063 .1

1064 Tiira, J., Moisseev, D. N., Von Lerber, A., Ori, D., Tokay, A., Bliven, L. F., &
1065 Petersen, W. A. (2016, sep). Ensemble mean density and its connection
1066 to other microphysical properties of falling snow as observed in Southern
1067 Finland. *Atmospheric Measurement Techniques*, 9(9), 4825–4841. Re-
1068 trieved from <https://www.atmos-meas-tech.net/9/4825/2016/> doi:
1069 10.5194/amt-9-4825-2016

1070 von Lerber, A., Moisseev, D., Bliven, L. F., Petersen, W. A., Harri, A. M., & Chan-
1071 drasekar, V. (2017). Microphysical properties of snow and their link to Ze-S
1072 relations during BA ECC 2014. *Journal of Applied Meteorology and Climatol-
1073 ogy*, 56(6), 1561–1582. doi: 10.1175/JAMC-D-16-0379.1

1074 Westbrook, C. D., Ball, R. C., Field, P. R., & Heymsfield, A. J. (2004a, aug). The-
1075 ory of growth by differential sedimentation, with application to snowflake for-
1076 mation. *Physical Review E - Statistical Physics, Plasmas, Fluids, and Related
1077 Interdisciplinary Topics*, 70(2), 7. Retrieved from [https://link.aps.org/
1078 doi/10.1103/PhysRevE.70.021403](https://link.aps.org/doi/10.1103/PhysRevE.70.021403) doi: 10.1103/PhysRevE.70.021403

1079 Westbrook, C. D., Ball, R. C., Field, P. R., & Heymsfield, A. J. (2004b). Univer-
1080 sality in snowflake aggregation. *Geophysical Research Letters*, 31(15). doi: 10
1081 .1029/2004GL020363

1082 Westbrook, C. D., & Sephton, E. K. (2017). Using 3-D-printed analogues to inves-
1083 tigate the fall speeds and orientations of complex ice particles. *Geophysical Re-
1084 search Letters*, 44(15), 7994–8001. doi: 10.1002/2017GL074130

1085 Woods, C. P., Stoelinga, M. T., & Locatelli, J. D. (2007, nov). The IMPROVE-1
1086 storm of 1-2 February 2001. Part III: Sensitivity of a mesoscale model sim-
1087 ulation to the representation of snow particle types and testing of a bulk
1088 microphysical scheme with snow habit prediction. *Journal of the Atmospheric
1089 Sciences*, 64(11), 3927–3948. Retrieved from [http://journals.ametsoc.org/
1090 doi/abs/10.1175/2007JAS2239.1](http://journals.ametsoc.org/doi/abs/10.1175/2007JAS2239.1) doi: 10.1175/2007JAS2239.1

1091 Zawadzki, I., Jung, E., & Lee, G. (2010, may). Snow studies. Part I: A study of nat-
1092 ural variability of snow terminal velocity. *Journal of the Atmospheric Sciences*,
1093 67(5), 1591–1604. Retrieved from [http://journals.ametsoc.org/doi/abs/
1094 10.1175/2010JAS3342.1](http://journals.ametsoc.org/doi/abs/10.1175/2010JAS3342.1) doi: 10.1175/2010JAS3342.1

1095 Zikmunda, J., & Vali, G. (1972, oct). Fall Patterns and Fall Velocities of Rimed
1096 Ice Crystals. *Journal of the Atmospheric Sciences*, 29(7), 1334–1347. doi: 10
1097 .1175/1520-0469(1972)029<1334:fpafvo>2.0.co;2

Supporting Information for "Ice Particle Properties Inferred from Aggregation Modelling"

M. Karrer¹, A. Seifert², C. Siewert², D. Ori¹, A. von Lerber^{1,3}, S. Kneifel¹

¹Institute for Geophysics and Meteorology, University of Cologne, Cologne, Germany

²Deutscher Wetterdienst, Offenbach, Germany

³Finnish Meteorological Institute, Helsinki, Finland

Contents of this file

1. Figures S1 to S9

Introduction

In this supplemental material we provide additional figures, which may be interesting for some readers but are not necessary to draw the conclusions of the main text. We show figures with the same or similar content than figures in the main text, but using a different size definition or additional monomer types.

Particle Properties Against Mass Equivalent Diameter

Figure S1 shows the same plot as Figure 7 but using the mass-equivalent diameter D_{eq} . This depiction might be helpful in applications where m is the primary variable (instead of D_{max}). Overall Figure 7 and Figure S1 look similar and we do not observe systematic shifts in the dependency of v_{term} on N_{mono} when changing the variable.

Dependence of Aggregate Mass, Area and Terminal Velocity on Monomer Number for Additional Monomer Types

Figures S2 and S5 show the particle properties m and A and Figure S3 and S5 show v_{term} of dendrites and columns. While dendrites behave similarly to plates (both are planar-like shapes), columns behave similar to needles (both are column-like shapes). For dendrites m , A and v_{term} is decreasing with increasing N_{mono} . For columns m , A and v_{term} is increasing with increasing N_{mono} .

Power Law and Atlas-type Fits for Terminal Velocity for Additional Monomer Types

Figures S6 to S10 show power law and Atlas-type fits for monomers and aggregates for needles, dendrites, columns as well as the mixture of columns and dendrites ("Mix1" and "Mix2"). For the mixtures "Mix1" and "Mix2" $N_{mono} = 1$ is defined by the properties of the column monomer. Also for these habits, the Atlas-type fit allows a much more accurate representation of v_{term} at large sizes. The deviation between the assumptions in the microphysics schemes and the dendrites is especially large. The monomers and aggregates of columns and "Mix2" (which assume monomers with $D_{max} < 1mm$ to be columns and monomers with $D_{max} > 1mm$ to be dendrites) exhibit larger values of v_{term} which is closer to the assumptions in the microphysics schemes. "Mix2" (here the selection of the monomer type - dendrite or column - is random) shows a large spread of v_{term} of the individual particles.

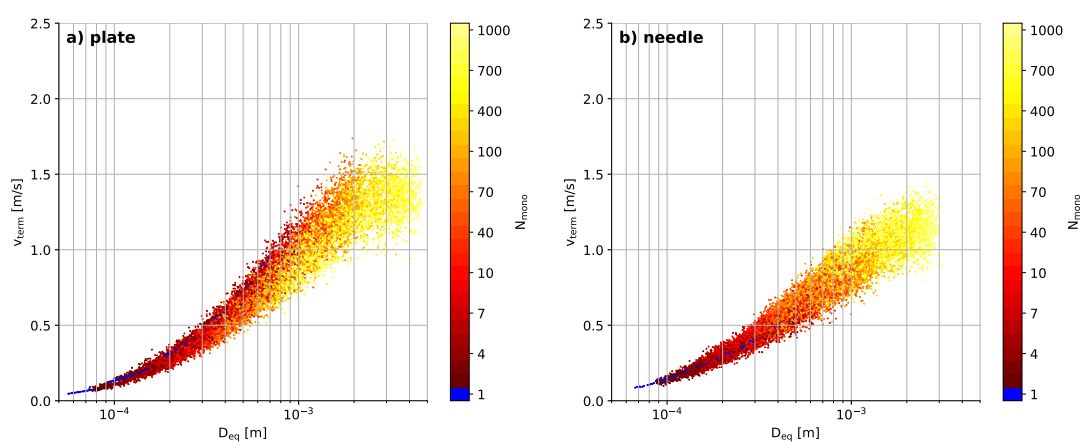


Figure S1. Same as Figure 7 but using the mass-equivalent diameter D_{eq} . Fits for different values of N_{mono} have not been calculated.

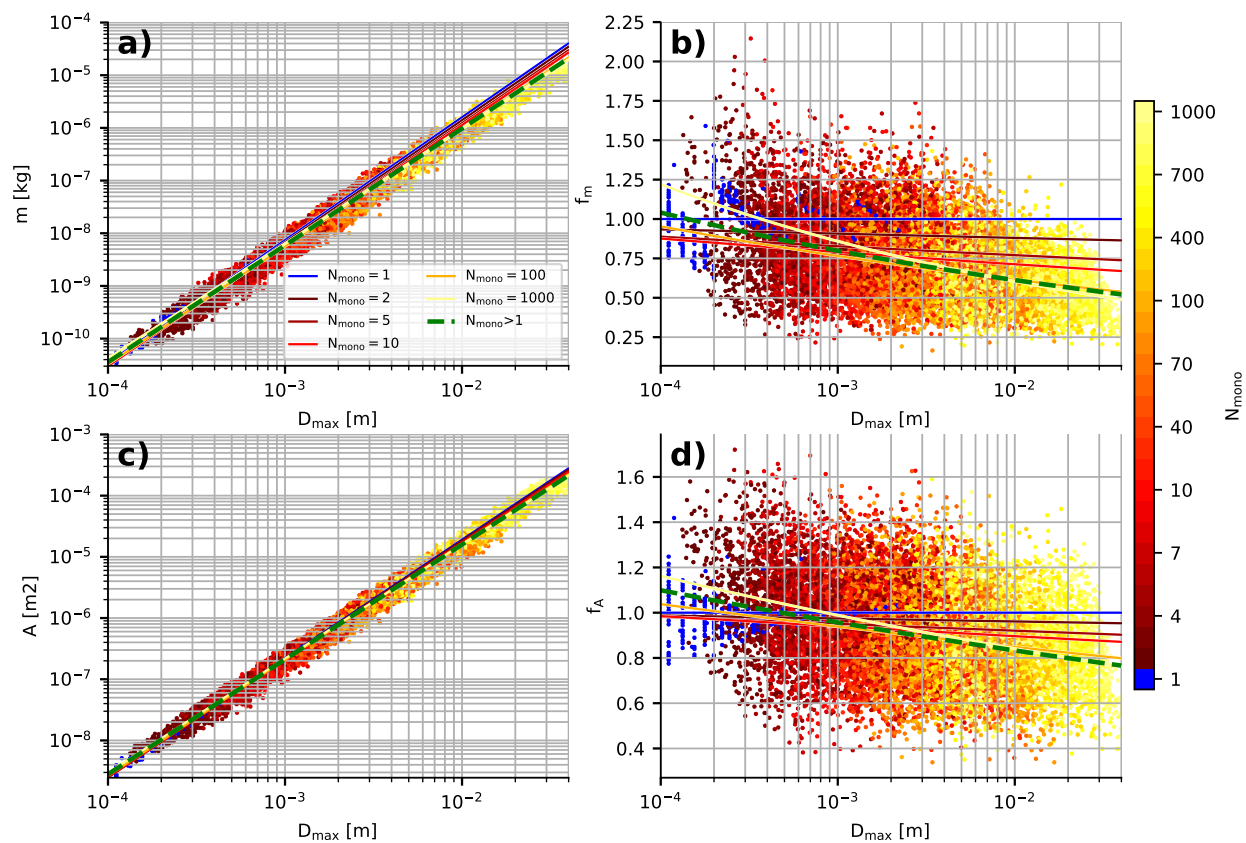


Figure S2. Same as Figure 6 but for aggregates of dendrites

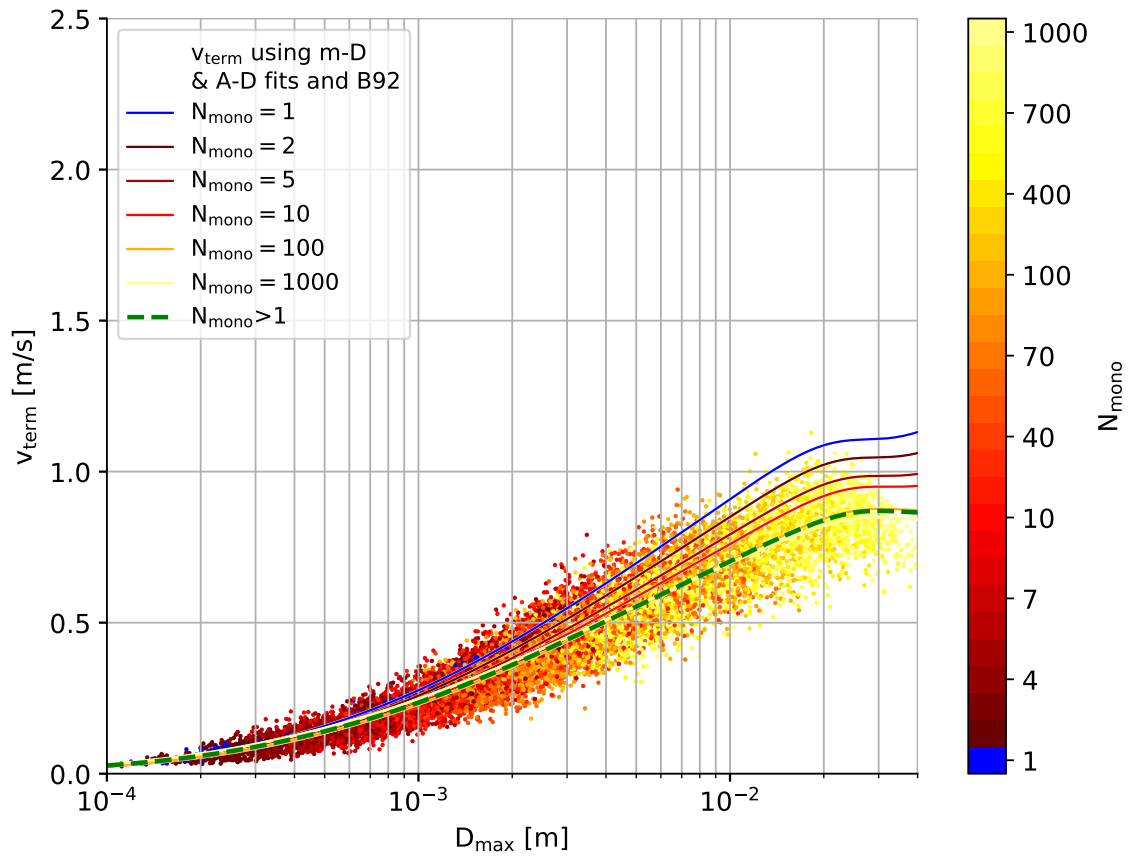


Figure S3. Same as Figure 7 but for aggregates of dendrites

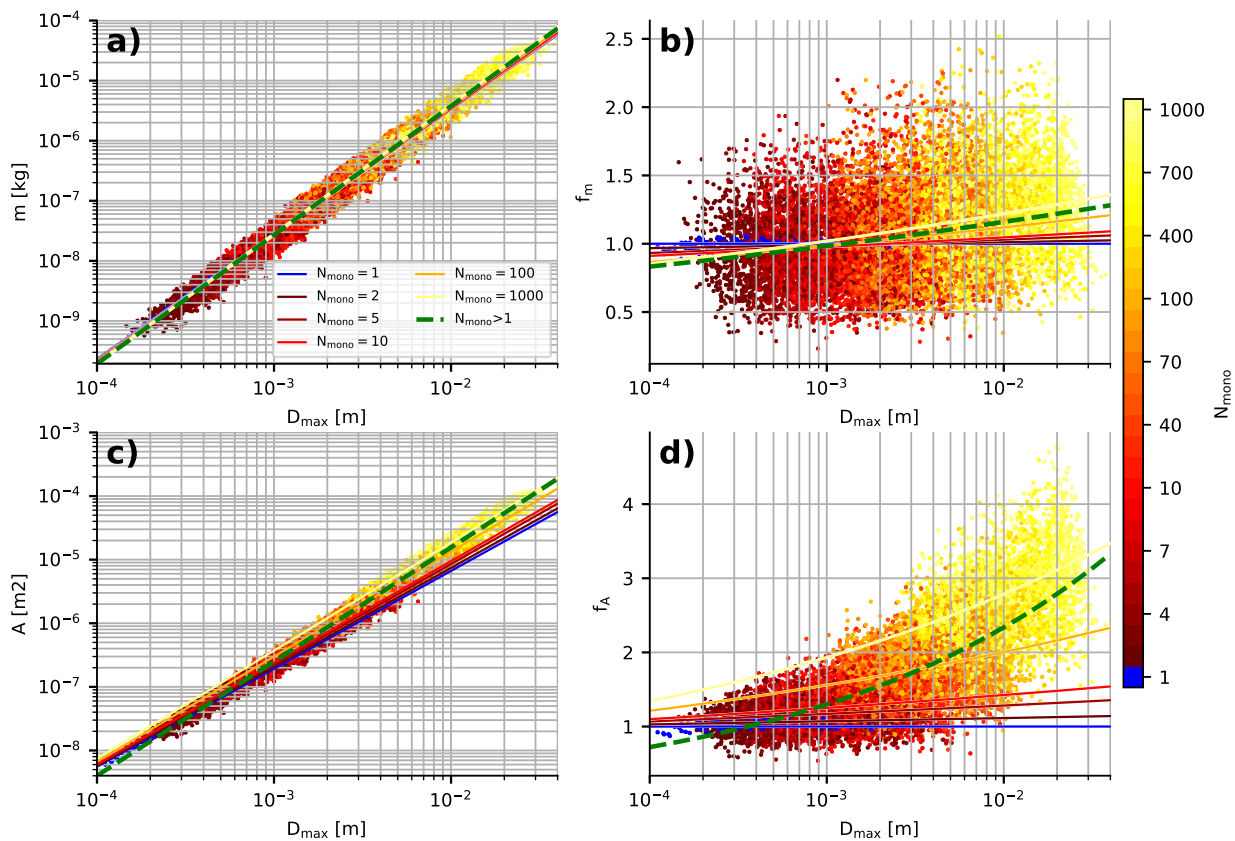


Figure S4. Same as Figure 6 but for aggregates of columns

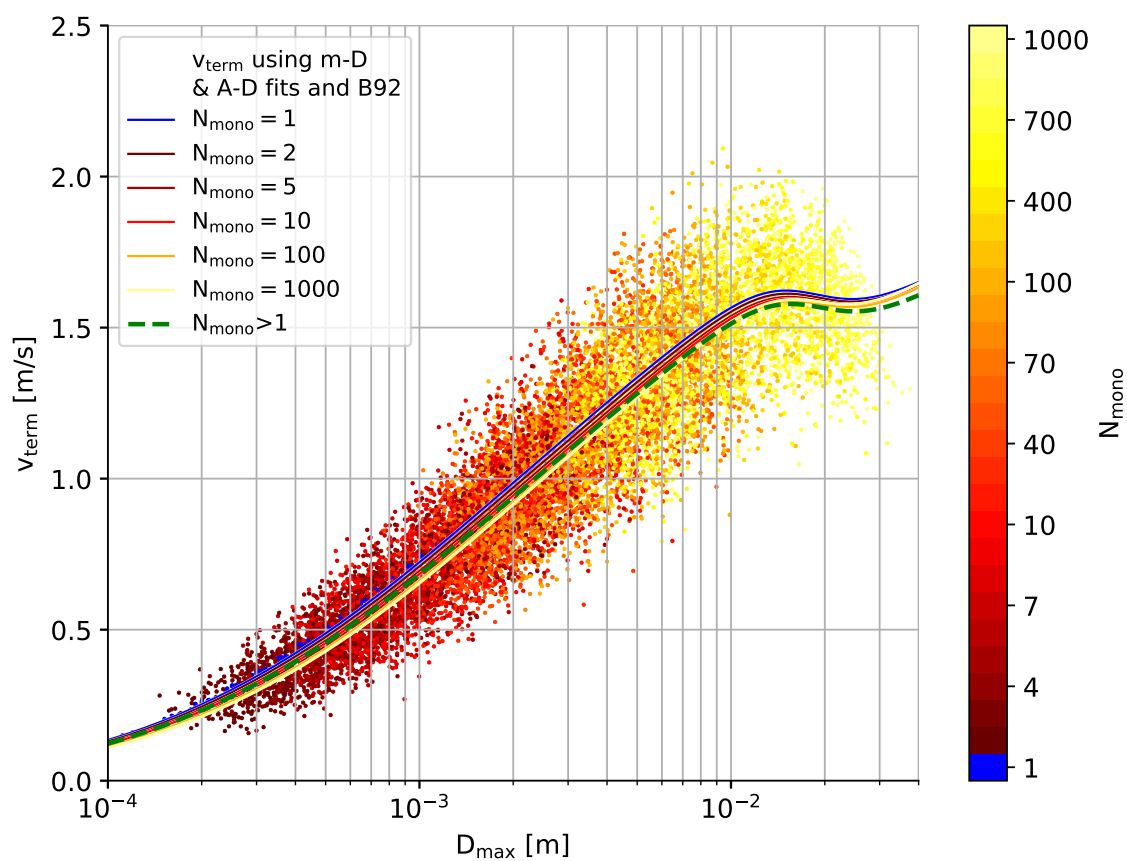


Figure S5. Same as Figure 7 but for aggregates of columns

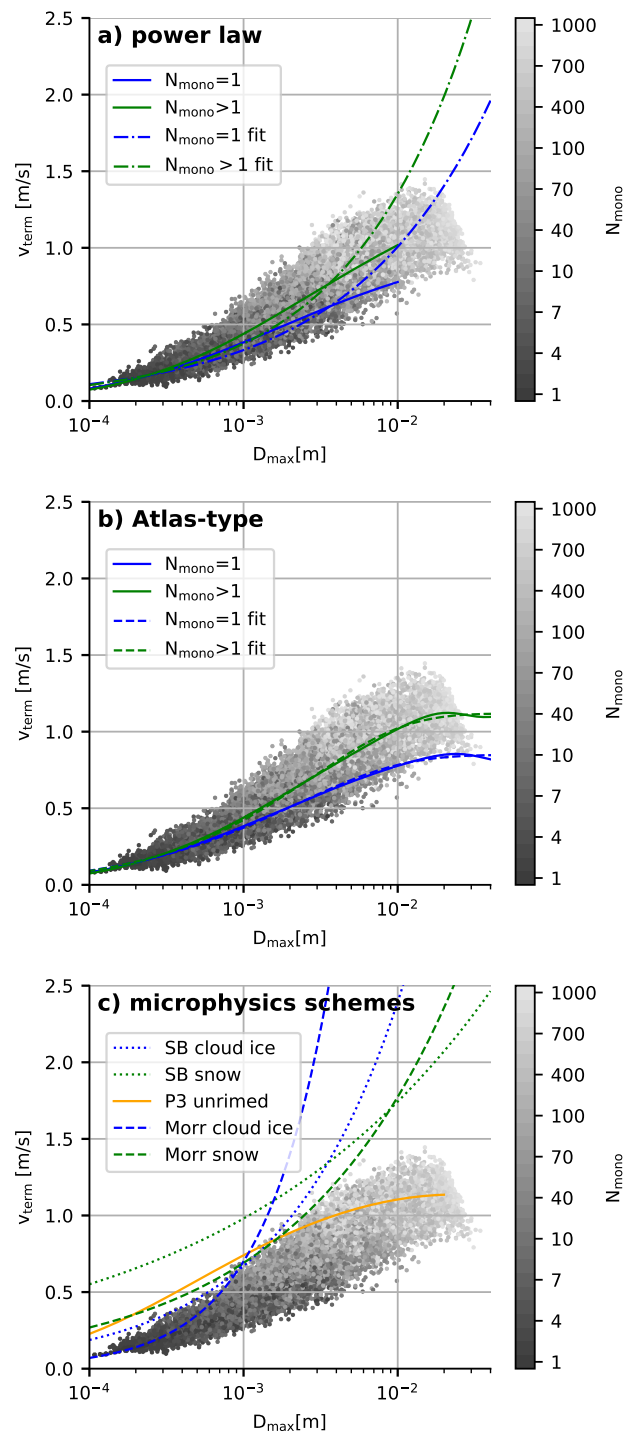


Figure S6. Same as Figure 9 but for aggregates of needles

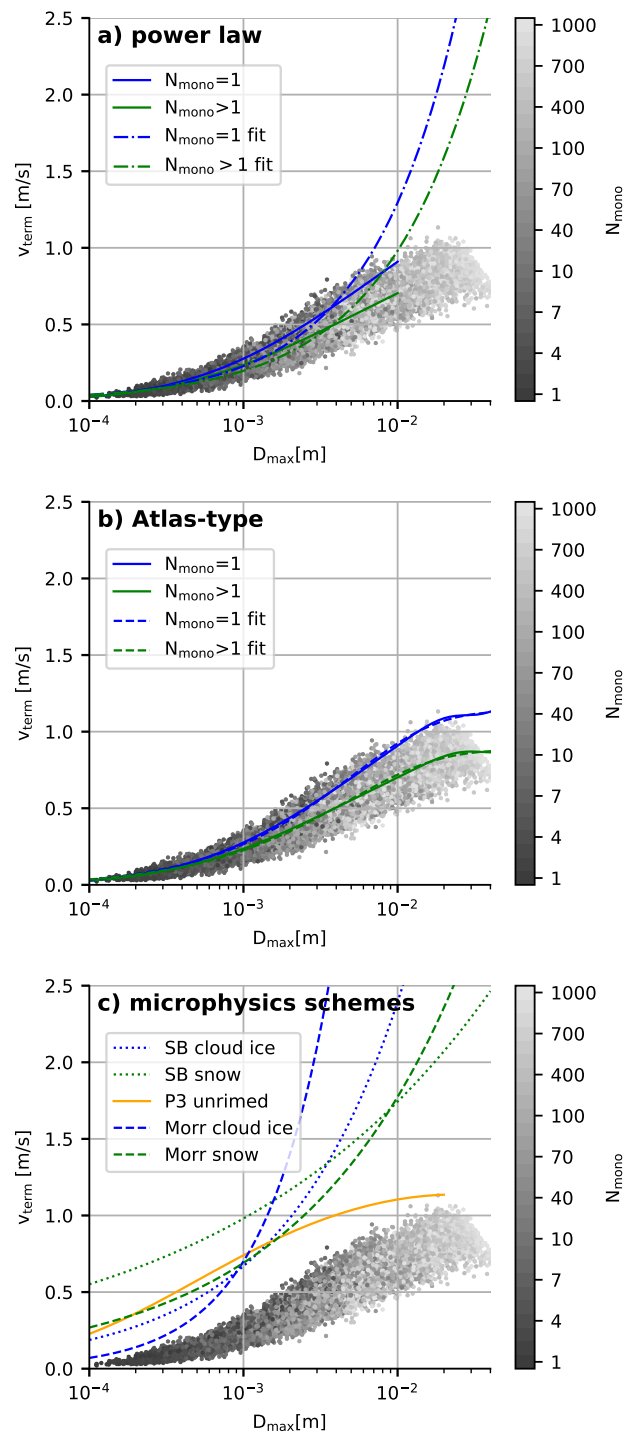


Figure S7. Same as Figure 9 but for aggregates of dendrites

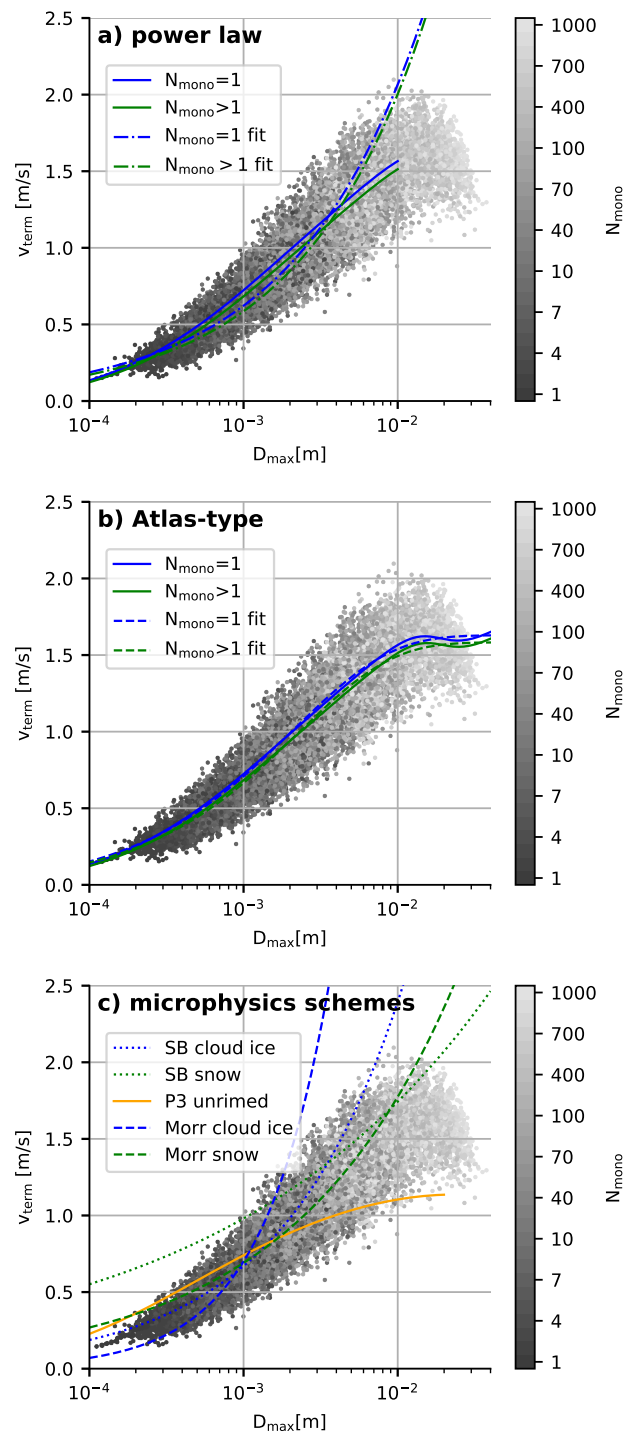


Figure S8. Same as Figure 9 but for aggregates of columns

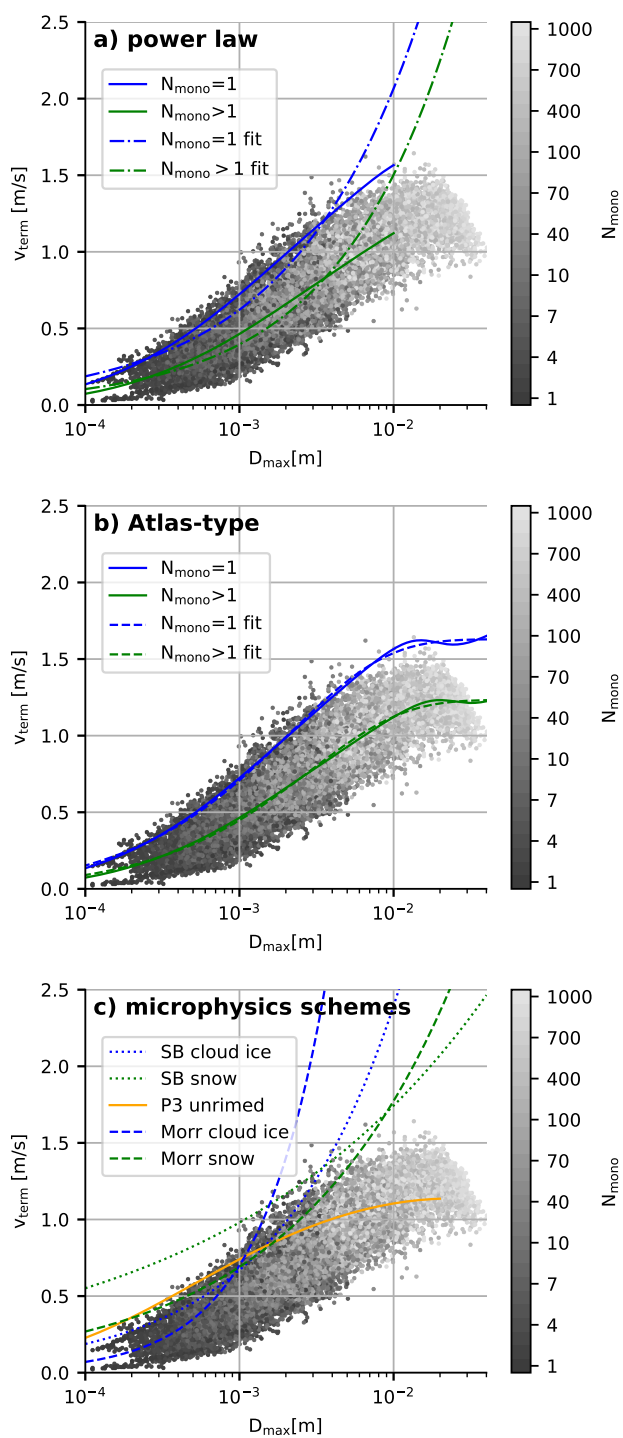


Figure S9. Same as Figure 9 but for "Mix1"

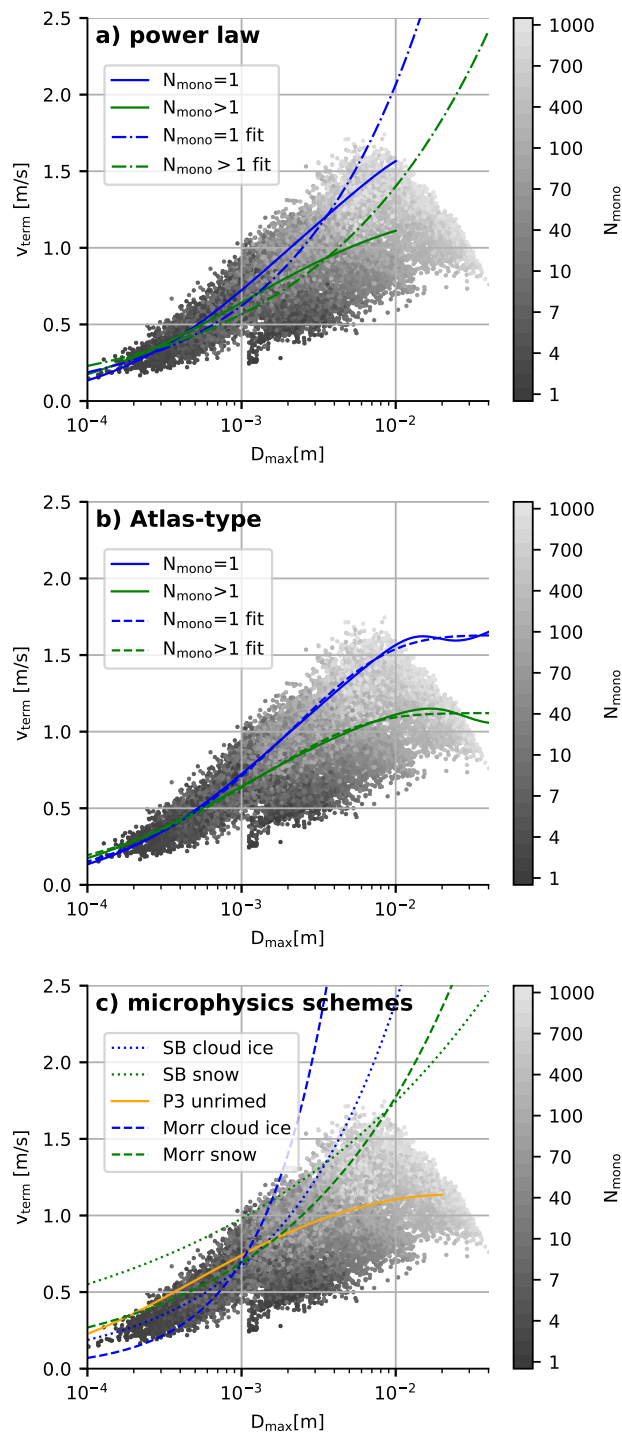


Figure S10. Same as Figure 9 but for "Mix2"